Journal of Medicinal Chemistry

Article

pubs.acs.org/jmc

Structure-Based Design and Development of Functionalized Mercaptoguanine Derivatives as Inhibitors of the Folate Biosynthesis Pathway Enzyme 6-Hydroxymethyl-7,8-dihydropterin Pyrophosphokinase from *Staphylococcus aureus*

Matthew L. Dennis,[†,‡] Sandeep Chhabra,[†,‡] Zhong-Chang Wang,[†,§] Aaron Debono,[†] Olan Dolezal,[‡] Janet Newman,[‡] Noel P. Pitcher,[†] Raphael Rahmani,[†] Ben Cleary,[†] Nicholas Barlow,[†] Meghan Hattarki,[‡] Bim Graham,[†] Thomas S. Peat,[‡] Jonathan B. Baell,[†] and James D. Swarbrick*[,†]

[†]Monash Institute of Pharmaceutical Sciences, Monash University, Parkville, Victoria 3052, Australia

[‡]CSIRO Biosciences Program, Parkville, Victoria 3052, Australia

[§]State Key Laboratory of Pharmaceutical Biotechnology, Nanjing University, Nanjing 210093, People's Republic of China

Supporting Information

ABSTRACT: 6-Hydroxymethyl-7,8-dihydropterin pyrophosphokinase (HPPK), an enzyme from the folate biosynthesis pathway, catalyzes the pyrophosphoryl transfer from ATP to 6-hydroxymethyl-7,8-dihydropterin and is a yet-to-be-drugged antimicrobial target. Building on our previous discovery that 8-mercaptoguanine (8MG) is an inhibitor of *Staphylococcus aureus* HPPK (SaHPPK), we have identified and characterized the binding of an S8-functionalized derivative (**3**). X-ray structures of both the SaHPPK/**3**/cofactor analogue ternary and the SaHPPK/cofactor analogue binary complexes have provided insight into cofactor recognition and key residues that move over 30 Å upon binding of **3**, whereas NMR measurements reveal a partially plastic ternary complex active site. Synthesis and binding analysis of a set of analogues of **3** have identified an advanced new lead compound (**11**) displaying >20-fold higher affinity for SaHPPK than 8MG. A number of these exhibited low micromolar affinity for dihydropteroate synthase (DHPS), the adjacent, downstream enzyme to HPPK, and may thus represent promising new leads to bienzyme inhibitors.

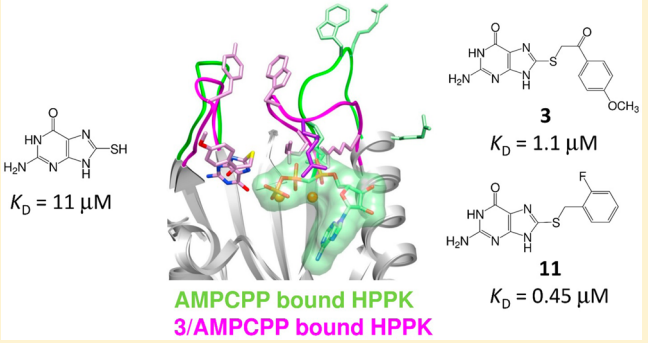

INTRODUCTION

Folate is an essential vitamin for the growth of all living organisms. The reduced form, tetrahydrofolate, is a critical cofactor for one-carbon transfer reactions required for the synthesis of purines, amino acids, S-adenosylmethionine, thymidine monophosphate, and formyl-methionine.[1,2] Mammals and higher eukaryotes depend on dietary folate, whereas plants and most microorganisms synthesize it de novo. The sulfa drugs, targeting the folate pathway enzyme dihydropteroate synthase (DHPS), are still used in the clinic after several decades and vindicate the pathway as an attractive source of antimicrobial targets.[3] Even today, sulfonamides are coadministered with a bacterial dihydrofolatereductase (DHFR) inhibitor as a synergistic broad-spectrum cocktail to prevent or treat a range of diseases and infections, including malaria, *Toxoplasma gondii* encephalitis, *Pneumocystis carinii* pneumonia, Tuberculosis, and *Staphylococcus aureus* infections.[4−8]

Point mutations in both DHPS[9] and DHFR[10] genes have led to resistance to sulfamethoxazole (SMX)- and trimethoprim (TMP)-based therapies, respectively. Structure-based rational design has therefore sought new generations of lead compounds effective on DHFR mutant strains[11] as well as the possibility of more tailored sulfa drugs,[12] novel pterin-site binding motifs,[9,13] and allosteric inhibitors of DHPS.[14] Recent insights into the structural basis for the off-target side effects of the sulfa drugs[15] are likely to assist in improving the selectivity and efficacy of this class of drug.

Notwithstanding these efforts, the magnitude of the problem of antibiotic resistance is highlighted by the emergence of the methicillin-resistant strains of *S. aureus* (MRSA) ("the super bug"). Originally confined within the hospital setting, more recently it has spread to the community and begun affecting those without any risk factors.[16,17] The search for effective future treatments has resulted in increasing interest into alternative enzyme targets for new antibacterials[18] as well as novel immunization strategies.[19] In this regard, our own research[20,21] has focused on the structure-based development of inhibitors of

Received: August 21, 2014

   dx.doi.org/10.1021/jm501417f | *J. Med. Chem.* XXXX, XXX, XXX−XXX

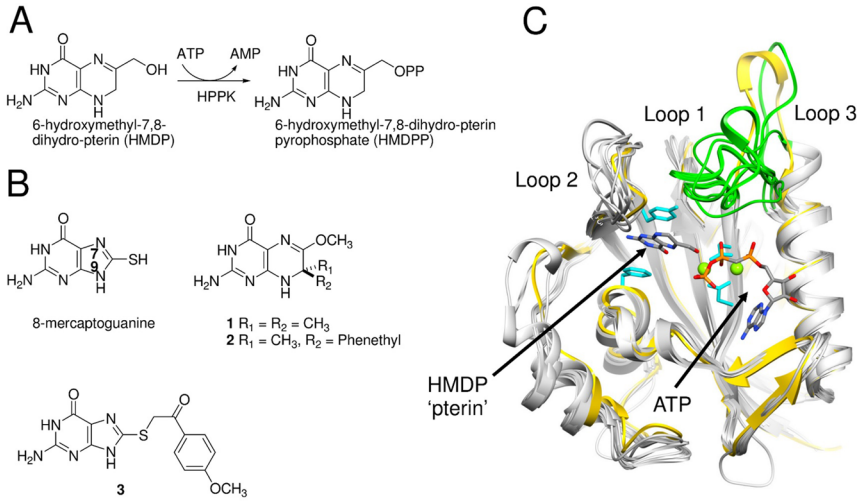

Figure 1. (A) HPPK catalysis. (B) Structures of selected HPPK inhibitors. (C) Superposition of EcHPPK structures (gray) with the SaHPPK/8MG structure (PDB: 3QBC, yellow) showing active site loop conformations in response to a variety of bound ligands along with the bound substrate (HMDP) and cofactor analogue (AMPCPP). Observed loop 3 conformational changes for EcHPPK are highlighted in green.

6-hydroxymethyl-7,8-dihydropterin pyrophosphokinase (HPPK), the enzyme directly preceding DHPS in the folate pathway, responsible for catalyzing pyrophosphoryl transfer from a magnesium-bound ATP cofactor to 6-hydroxymethyl-7,8-dihydro-pterin (HMDP) (Figure 1A). HPPK is not a known target for any existing antibiotic, has no relevant human homologues, and has druggable sites to develop antimicrobials effective on current and future SMX/TMP-resistant pathogens.

HPPK is an 18 kDa enzyme composed of a three-layered $\alpha-\beta-\alpha$, thioredoxin-like fold (Figure 1).[22] Catalysis follows an ordered mechanism, whereby the ATP cofactor binds initially to a comparatively open pocket in which the triphosphate is complexed by two magnesium ions that are additionally coordinated by two highly conserved aspartic acid residues.[23] Binding of the HMDP substrate then follows, stacking between two conserved aromatic rings. Three loops (loops 1−3, Figure 1) interact and seal the active site to allow pyrophosphate transfer from the cofactor to the substrate. A large body of structural data,[22] predominantly for the *Escherichia coli* enzyme (EcHPPK) with the nonhydrolyzable cofactor analogue, AMPCPP, reveals a relatively rigid core structure and flexible loops, particularly the cofactor loop 3, which undergoes a mechanistically important 20 Å positional change during the catalytic cycle.[23,24] X-ray structures of HPPK from several species[21,25−28] reveal highly conserved residues in the active site, indicating that suitably designed inhibitors could display broad-spectrum activity.

Only a few inhibitors of HPPK have been reported to date. Early work, predating the structural characterization of HPPK, led to the identification of the gem dimethyl- (**1**) and phenethyl-substituted (**2**) substrate analogues as inhibitors (Figure 1).[29] Rationally designed bisubstrate analogues based on these have also been reported.[30−32] Recently, adopting a rapid overlay of chemical similarity (ROCS) scaffold hopping screening method, we measured the binding of a series of commercially available substrate-like compounds and identified 8-mercaptoguanine (8MG) (Figure 1B) as a novel inhibitor of the *S. aureus* enzyme (SaHPPK) (K_D = 11 μM, IC_{50} = 41 μM).[21] Unlike other inhibitors of HPPK, binding of this compound was shown to be independent of cofactor and Mg^{2+} ions. 8MG benefits from a high level of steric and electronic complementarity to the substrate site and being small, resulting in a high ligand efficiency rating (ΔG/number of heavy atoms = 0.63 kcal mol^{-1} heavy $atom^{-1}$). On the basis of this discovery, we initiated an ongoing SAR program to structurally elaborate 8MG into a more potent inhibitor.[20] Because of the demonstrated importance of the sulfur substituent, we initially focused on chemical extension from the N9 and N7 positions, revealing that only the latter strategy was viable. An N7-ethyl alcohol variant exhibited comparable affinity to that of the parent compound, but it was competitive with the cofactor.

In view of the above findings, we decided to revisit extension from the sulfur atom of 8MG. This article reports the results of this latest work, which has culminated in the identification of several novel 8MG analogues displaying significantly higher affinities ($K_D \sim 0.45$ μM) for SaHPPK compared to that of the parent compound in the presence of saturating levels of cofactor. The SaHPPK binding ability and inhibitory activity of an initial lead compound, as well as a series of synthesized analogues, have been quantified by surface plasmon resonance (SPR) experiments and an in vitro luminescent kinase coupled-enzyme assay, respectively, and important structural and dynamic features of the lead/cofactor/SaHPPK ternary complex have been revealed by heteronuclear NMR spectroscopy. By solving the X-ray structure of this complex, the intermolecular interactions between the lead inhibitor and the enzyme have also been delineated. Additionally, the X-ray structure of the wild-type SaHPPK with a cofactor analogue bound has been determined, revealing key residues required for cofactor recognition and those that have moved by over 30 Å upon binding of the inhibitor. Finally, SPR data is presented that show that a number of the new 8MG analogues are also able to bind to DHPS with low micromolar affinity, indicating the potential of this class of compound to be developed into dual-action enzyme inhibitors.[33]

RESULTS AND DISCUSSION

A simple similarity search based on the TimTec (www.timtec.net) catalogue was performed, and the four commercially available 8MG analogues (out of seven hits) were purchased: 8-*N*-morpholinoguanine, 7-methylguanine, 8-bromoguanine, and 8-((2-(4-methoxyphenyl)-2-oxoethyl)thio)guanine (**3**). The SaHPPK binding properties of the first three of these compounds were reported in our earlier work.[20] Compound **3** is reminiscent

dx.doi.org/10.1021/jm501417f | J. Med. Chem. XXXX, XXX, XXX−XXX

of the known 7-methyl-7-phenethylpterin analogue (**2**) of Wood et al.[29] (Figure 1B), which was crystallized, along with the 7-gemdimethyl variant (**1**), in the first EcHPPK structure by Stammers et al.[34]

Binding of 3 to SaHPPK by SPR. Binding of **3** to SaHPPK was initially quantitatively analyzed by SPR, with SaHPPK immobilized on a nitrilotriacetic acid (NTA) sensor chip surface. Binding sensorgrams (Figure 2) were of good quality and

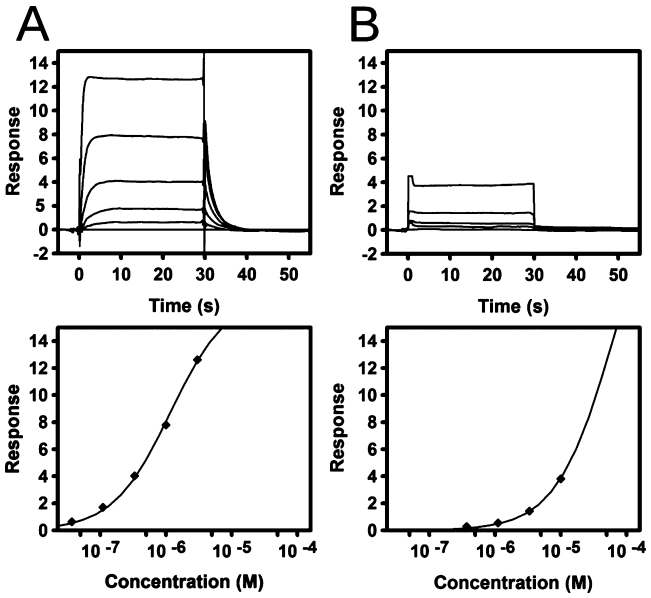

Figure 2. SPR sensorgrams (top panels) and steady-state affinity fits (bottom panels) for the binding of compound **3** to SaHPPK in the (A) presence or (B) absence of 1 mM ATP.

consistent with 1:1 stoichiometric binding. The binding affinities (K_D values) were derived by globally fitting the steady-state data sets to a single-site binding model. Thus, in the presence of ATP, **3** was estimated to bind SaHPPK with an affinity of 1.09 ± 0.12 μM. On the other hand, in the absence of ATP, steady-state fitting using 8MG as a reference (K_D = 10.8 ± 0.4 μM)[21] revealed far weaker binding (K_D = 77 ± 16 μM).

Binding of 3 to SaHPPK by NMR Spectroscopy. The chemical shift of a nucleus is highly sensitive to changes in its local environment and is thus a convenient site-specific probe for analyzing ligand-binding events, including conformational and dynamic changes during complex formation.[35] Incremental addition of **3** to a sample of apo SaHPPK revealed only moderate strength binding, as evidenced by signal broadening (characteristic of intermediate exchange) and very minor chemical shift perturbations (CSPs) (data not shown). Broadened resonances mapped approximately to the substrate-binding site (data not shown). In stark contrast, titration of **3** into a solution of SaHPPK with either ATP or the nonhydrolyzable ATP analogue, AMPCPP, fully bound resulted in widespread chemical shift changes (Figure 3A), and all CSPs exhibited slow exchange on the NMR time scale. Moreover, in contrast to the case with 8MG,[21] saturation was achieved at close to a 1:1 ligand-to-enzyme ratio, consistent with the higher affinity of **3** for SaHPPK measured by SPR (vide supra) in the presence of the nucleotide.

To investigate the binding of **3** in more detail, we assigned the ^{1}HN, ^{15}N, and ^{13}CA backbone resonances for the **3**/AMPCPP/SaHPPK ternary complex using a triple-resonance 3D NMR experiment. The absolute CSPs induced by binding of **3** to the AMPCPP bound SaHPPK were distributed mainly over two regions that, when mapped to the structure (Figure 3D), are consistent with pterin-site binding. Amides 8−12 on the sheet lining the pterin pocket showed small absolute CSPs around the one-standard deviation (σ) value (Figure 3B). Amides from residues 44−53 in loop 2 that are more solvent-exposed (see green or surface representation) and the more buried ring stacking amide from Phe123 showed even larger CSPs, over 3σ in magnitude. Other large CSPs were also observed for Gly90, Cys80, His82, and the side-chain Hε2 of His115 in the loop 3 hinge region, which probably reflect changes in loop structure between the AMPCPP/SaHPPK binary and **3**/AMPCPP/SaHPPK ternary complexes. Although the structure of the 8MG/AMPCPP/SaHPPK complex has yet to be determined, a similarly large CSP is observed for Gly90 upon the addition of 8MG (Figure 3A), suggesting that the position and environment of the tip of loop 3 in this structure is similar to that in the **3**/AMPCPP/SaHPPK complex, at least around the Gly90 position.

In order to specifically probe the binding mode of the S8-substituted pendant in **3**, together with any associated conformational changes in the SaHPPK structure, the CSPs for the **3**/AMPCPP/SaHPPK complex were compared to those derived from the 8MG/AMPCPP/SaHPPK spectra (Figure 3C) and depicted in a model constructed from the AMPCPP/SaHPPK X-ray structure (vide infra). As part of this initial analysis, it was assumed that the guanine moieties of 8MG and **3** superpose in the substrate pocket, and the loop 2 conformation was derived from that observed in the 8MG/SaHPPK binary complex.[21] Differential CSP data is quite powerful for determining the pose of bound ligands by NMR,[36] and this analysis showed that the pendant of **3** interacts closely with residues in loop 2, specifically around Tyr48, extending up and out from the base of the substrate-binding site (Figure 3D). The differential CSP observed for Arg121 may be suggestive of a direct interaction with the pendant. The differential CSPs that mapped to those residues under the pterin pocket (amides 8−10), remote from the pendant, may support a small change in the binding orientation of the guanine moiety compared to that in the 8MG/AMPCPP/SaHPPK case. Although Asp95 and His115 are not solvent-exposed, the changes in the CSPs reflect a change in the environment near the gamma phosphate, potentially due to loop 3 structural changes (vide infra).

X-ray Structures of 3/AMPCPP/SaHPPK and AMPCPP/SaHPPK. The X-ray structure of SaHPPK in complex with **3** and AMPCPP (Figure 4) was solved at 2.0 Å resolution using molecular replacement (Table 1). The ternary complex crystallized in the $P6_1$ space group, with a single protein molecule in the asymmetric unit. Backbone density was observed for all 158 amino acid residues of the protein. The guanine moiety of **3** is positioned similarly to that of 8MG in the 8MG/SaHPPK binary complex,[21] making a total of six hydrogen bonds with the protein and π-stacking between the aromatic rings of Phe54 and Phe123. The aromatic ring of the pendant projects out and away from the substrate pocket into the loop 2/loop 3 region, making favorable hydrophobic interactions with Val46 and Gly47. The adjacent ketone group stacks against the guanidinium group of Arg121 and also interacts with the phenyl ring of Phe123. These features are also consistent with the large CSPs observed for these residues upon formation of the ternary complex (vide supra).

The Mg^{2+} ions in the **3**/AMPCPP/SaHPPK structure superpose closely with those in the HMDP/AMPCPP/EcHPPK structure (PDB: 1QON),[22,23] differing in position by only 0.22 (Mg1) and 0.35 Å (Mg2). Both ions are coordinated to residues

dx.doi.org/10.1021/jm501417f | J. Med. Chem. XXXX, XXX, XXX−XXX

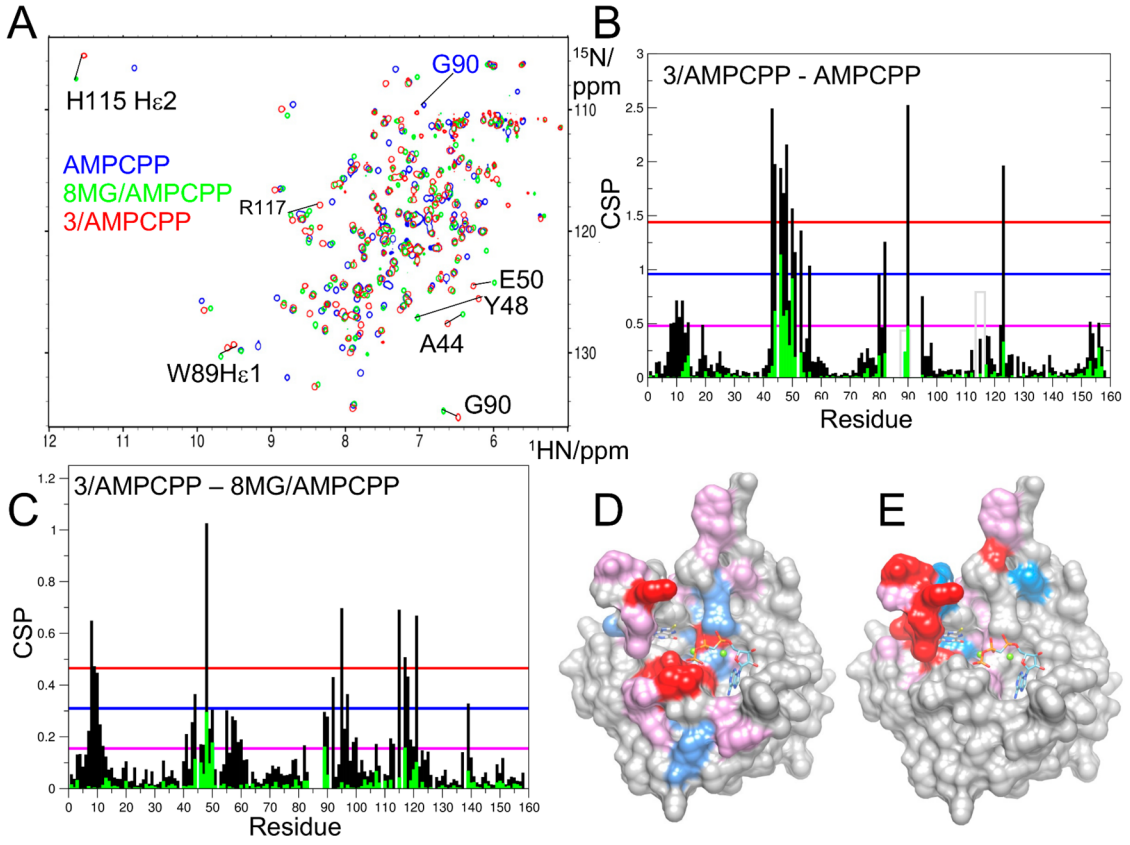

Figure 3. NMR data of SaHPPK binding to **3**. (A) Superposition of the 2D ^{15}N HSQC spectra recorded in a sample of ~120 μM SaHPPK in 10 mM Mg^{2+} 50 mM HEPES, pH 8, in the presence of saturating amounts of AMPCPP (blue), 8MG (green), and compound **3** (red). (B) Raw CSP (black) for the change in weighted averaged chemical shifts for **3**/AMPCPP compared to the AMPCPP 2D ^{15}N HSQC spectra. CSP plot weighted by solvent accessibility (green). CSPs for the side chain of His115 and Trp89 are shown in gray. (C) Raw weighted average chemical shifts (black) derived from the change in the **3**/AMPCPP and the 8MG/AMPCPP 2D NMR spectra and weighted for solvent accessibility (green). In both panels B and C, pink, blue, and red horizontal lines signify 1, 2, and 3 standard deviations of the CSPs. (D, E) CSPs greater than the values in panels B and C are mapped to the structure of SaHPPK in panels D and E, respectively.

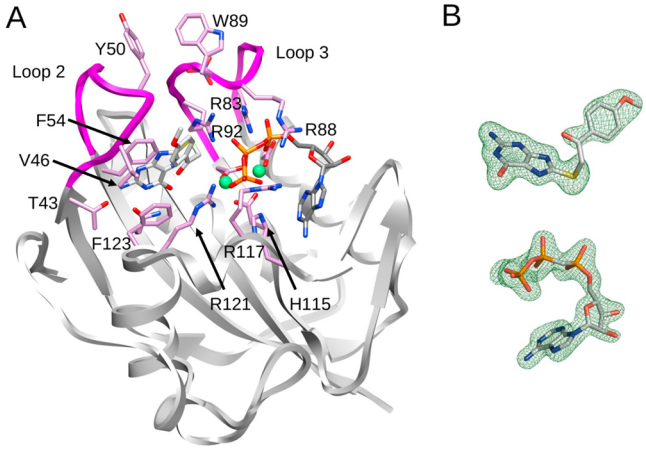

Figure 4. X-ray structure of SaHPPK in complex with AMPCPP and **3**. (A) Detail of the active site. Loops 2 and 3 are shown in magenta, and the two magnesium ions, in green. (B) mF_o − DF_c difference density map of AMPCPP and 8MG contoured at 3.0σ.

D95 and D97 and share coordination to a β-phosphate oxygen. One magnesium center is coordinated by the α-phosphate, whereas the other is bound by the γ-phosphate. The fifth and sixth coordination sites are occupied by water molecules in each case.

To help rationalize the conformational changes accompanying binding of **3**, as well as the ~70-fold enhanced affinity of **3** for the cofactor/SaHPPK complex relative to that for SaHPPK alone, the X-ray structure of SaHPPK in complex with AMPCPP was also determined (Figure 5). The complex crystallized in the space group $P2_1$ (Table 1) and was solved via molecular replacement to a resolution of 2.7 Å. In contrast to the 8MG/SaHPPK complex, four rather than two protein molecules were found in the asymmetric unit (Figure 5A).[21] There are also differences between the two crystal forms in terms of the nature of the protein−protein interface. The existence of an intermolecular disulfide bond between the solvent-exposed Cys80 residues of neighboring proteins in the AMPCPP/SaHPPK crystal lattice is particularly notable (Figure 5B). Despite the presence of AMPCPP in the crystallizing solution used to grow crystals of the 8MG/SaHPPK binary complex, AMPCPP did not bind in this case, which was rationalized in terms of the binding site being partly occluded by the interface of the protomers in the asymmetric unit. The change in the nature of the protein−protein interface associated with intermolecular disulfide bond formation appears to be more compatible with AMPCPP binding.

As anticipated, the AMPCPP occupies the cofactor site, with phosphate oxygens hydrogen-bonded to Arg121, Arg117, His115, and Arg92 (one of three arginines in loop 3). The adenine base is hydrogen-bonded to the amide backbone of Ile98

dx.doi.org/10.1021/jm501417f | J. Med. Chem. XXXX, XXX, XXX−XXX

Table 1. X-ray Statistics

	AMPCPP (4CYU)	AMPCPP/**3** (4CRJ)	AMPCPP/**7** (4CWB)
spacegroup	$P2_1$	$P6_1$	$P6_1$
wavelength (Å)	1.0080	0.9537	0.9537
unit-cell parameters (Å, deg)	a = 62.00, b = 94.26, c = 62.99, $\alpha = \gamma$ = 90.00, β = 112.44	$a = b$ = 82.48, c = 52.17, $\alpha = \beta$ = 90.00, γ = 120.00	$a = b$ = 83.82, c = 52.04, $\alpha = \beta$ = 90.00, γ = 120.00
Diffraction Data			
resolution range (Å)	47.13−2.70 (2.77−2.70)	42.17−2.00 (2.05−2.00)	42.33−1.56 (1.60−1.56)
no. of unique reflections	18 506 (2455)	13 792 (1962)	29 793 (1419)
no. of observed reflections	139 533	296 051	332 946
Matthews coefficient, V_M (Å^3 Da^{1-})	2.39	2.83	2.93
solvent content (%)	48.6	58.6	58.1
completeness (%)	100.0 (100.0)	99.7 (98.0)	99.7 (96.9)
data redundancy	7.5 (7.6)	21.5 (19.7)	11.2 (10.3)
mean $I/\sigma(I)$	9.4 (2.1)	12.2 (3.6)	14.0 (2.7)
R_{merge}	0.139 (0.899)	0.215 (1.02)	0.091 (0.673)
$R_{p.i.m.}$	0.082 (0.528)	0.047 (0.232)	0.041 (0.315)
Refinement			
R_{free} (%)	24.2	20.0	17.8
R_{cryst} (%)	19.4	16.4	16.0
size of R_{free} set (%)	4.5	5.0	5.1
protein molecules in the asymmetric unit	4	1	1
inhibitor molecules		1	1
cofactor-analogue molecules	4	1	1
water molecules	13	83	141
RMSD from Ideal Values			
bond lengths (Å)	0.010	0.006	0.009
bond angles (deg)	1.49	1.36	1.60
Mean B factors (Å^2)	54.2	27.4	15.5
Ramachandran Plot			
favored (%)	99.0	98.7	98.2
outliers (%)	0.2	0.0	0.0

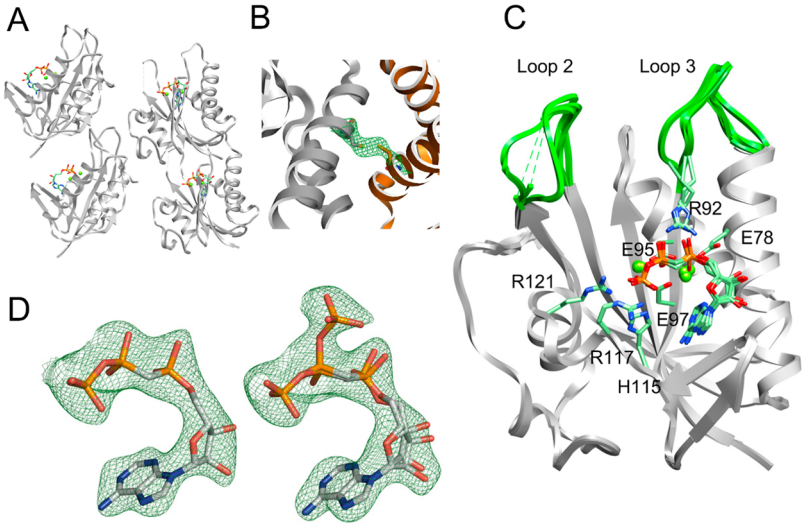

Figure 5. X-ray structure of SaHPPK in complex with AMPCPP. (A) X-ray structure showing the spatial arrangement of the four protomers in the asymmetric unit. (B) $2mF_o - DF_c$ standard density map (green mesh) contoured at 1.5σ showing a disulfide bond observed between protomers in adjacent unit cells. (C) $mF_o - DF_c$ difference density map (green mesh) of AMPCPP from protomers A (left) and B (right) contoured at 3.0σ. (D) Superposition of the four protomers and detail of the interactions of the bound AMPCPP. In panels A and C, alternate conformations of AMPCPP are omitted for clarity, and magnesium ions are colored green.

and Ser112 and forms hydrophobic contacts with the side chains of Leu111, Ile98, and Leu71. The ribose O2′ is hydrogen-bonded to Lys110. Two magnesium ions are again present, coordinated by Asp95, Asp97, and either the α- and β-phosphates or the β- and γ-phosphates of AMPCPP. Alternate conformations of AMPCPP are present in protomers B and D. In these conformations, the γ-phosphate is oriented orthogonal to the γ-phosphate site (Figure 5D), forming additional interactions to

dx.doi.org/10.1021/jm501417f | J. Med. Chem. XXXX, XXX, XXX−XXX

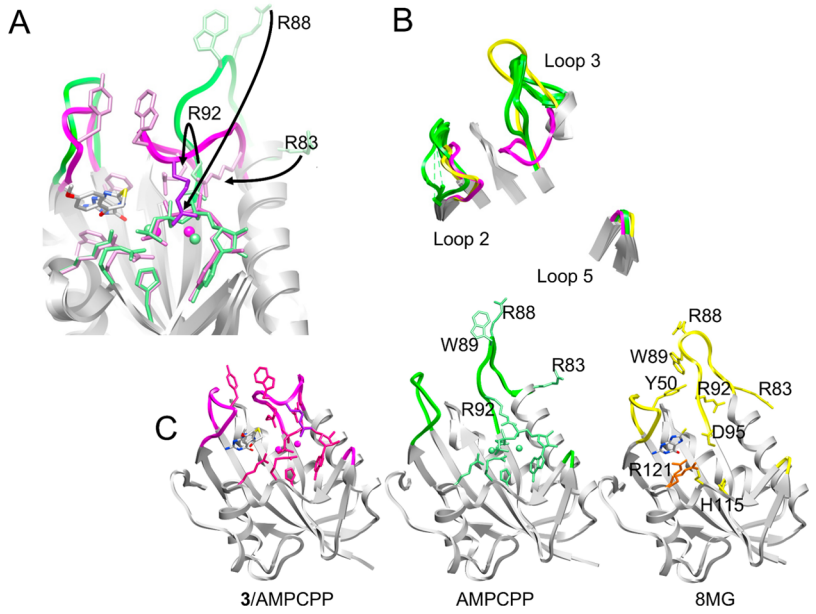

Figure 6. Conformational changes in SaHPPK. (A) Superposition of the AMPCPP (green) and the AMPCPP/**3** (magenta) X-ray structures illustrating the change in conformation of the loop 3 and selected arginine side chains. (B) Superposition of the three SaHPPK X-ray structures shown in panel C highlighting the changes in the loop regions. (C) Comparison of the X-ray structure of SaHPPK in complex with AMPCPP/**3**, AMPCPP, and 8MG. Selected side chains are shown to illustrate the positional and conformational changes.

Arg92 and Gln3 of an adjacent protomer, at the expense of loss of hydrogen bonds to His115, Arg118, and Arg121 as well as coordination to a magnesium ion.

Density was either weak or not observed for several of the loop 2 residues, indicative of mobility therein, concordant with prior NMR relaxation studies on EcHPPK[37] and SaHPPK[21] in which loop 2 was shown to be dynamic in the absence of bound substrate or substrate inhibitor. The observed loop 3 conformations (Figure 5C) overlap well with those previously found in the ensemble of NMR structures of AMPCPP/EcHPPK (data not shown),[24] and the existence of multiple conformations in the structure is again in line with the broadened NMR resonances observed for residues 84−89 and 92 (vide supra). In the AMPCPP complex, the side chain of Arg92 is extended and makes an end-on salt bridge to the α- and β-phosphates, which caused loop 3 to adopt a more open conformation relative to that observed in the crystal structure of apo EcHPPK.

It is noted that the side-chain orientation of Arg92 is not at all defined in the NMR structure of EcHPPK, which has been used in the past to represent the EcHPPK/AMPCPP structure in the absence of a suitable EcHPPK X-ray structure,[23] although this may reflect, to some degree, the difficulty and limitation of employing short-range NOEs to characterize hydrophilic interactions. The important role of Arg92 in cofactor recognition is underscored by the current AMPCPP/SaHPPK complex, which resembles the predicted AMPCPP/EcHPPK model derived from locally enhanced sampling and molecular dynamics simulations.[38]

A comparison of the two structures presented here with the previously reported 8MG/SaHPPK structure (PDB: 3QBC) (Figures 6A−C)[21] reveals marked differences in the conformation of the cofactor loop 3 and the substrate loop 2 and more subtle change in loop 5 (Figure 6B). There is a notable change in position of Arg92 upon binding of **3**. In the 8MG/SaHPPK structure, the guanidinium group of Arg92 is displaced by that of Arg83 and is translated 3.5 Å toward the substrate pocket. Arg83 moves 13 Å to make a hydrogen-bond contact to the α-phosphate. In the **3**/AMPCPP/SaHPPK complex, the Arg92 headgroup is also rotated by 90° and is oriented approximately parallel to that of Arg83; it hydrogen bonds to the β-phosphate as before. Gly90 at the tip of loop 3 moves ca. 17 Å closer to the active site upon the binding of **3** to the AMPCPP/SaHPPK complex. The conformations of the side chains of the other residues involved in nucleotide binding (Leu71, Leu75, Glu78, Asp95, Asp97, Ile98, Lys110, Leu111, Ser112, Val113, His115, and Arg117) do not change between the two structures.

The AMPCPP lies over 4 Å away from **3** in the ternary complex; therefore, the significantly enhanced binding affinity of **3** toward SaHPPK in the presence of the cofactor must be due to cofactor-induced intermolecular interactions rather than specific interactions with the cofactor itself. In the 8MG/SaHPPK structure,[21] residue Arg121 exists in two conformations (shown in orange in Figure 6C), one oriented toward and one perpendicular to the cofactor, suggesting that this residue is likely mobile in the apo enzyme. In both the AMPCPP/SaHPPK and **3**/AMPCPP/SaHPPK structures, the conformation appears to be locked by the hydrogen bond to the γ-phosphate of the AMPCPP, possibly assisted by a π interaction between the guanidinium group of Arg121 and the ketone of **3**, resulting in the observed cofactor-mediated improvement in binding affinity.

From the **3**/AMPCPP/SaHPPK structure, the large, yet similar, chemical shift change observed in the NMR spectra for Gly90 upon binding of **3** (Figure 3A) or 8MG to AMPCPP/SaHPPK can be attributed to hydrogen bonding to the carbonyl of Glu87 combined with a favorable interaction between the sulfur atom of each ligand and the carbonyl group of Trp89,[39] rather than a previously hypothesized hydrogen bond between the SH of 8MG and the carbonyl of Trp89.[21]

Insight into the Dynamics of the 3/AMPCPP/SaHPPK Complex by NMR. To investigate the dynamic properties of the **3**/AMPCPP/SaHPPK complex on the fast (pico- to nanosecond) time scale, ^{15}N heteronuclear NOEs were measured, and those amides with NOE values chosen to be less than 0.75 were mapped onto the surface of the structure (Figure 7) to highlight

dx.doi.org/10.1021/jm501417f | J. Med. Chem. XXXX, XXX, XXX−XXX

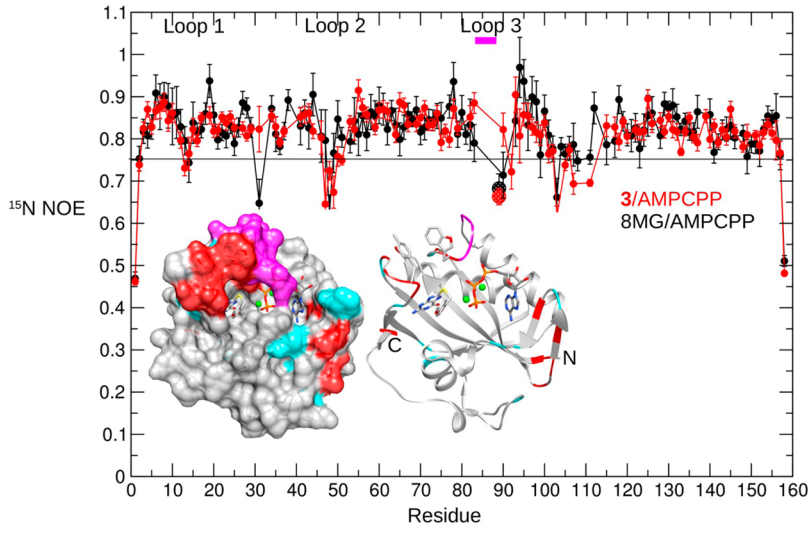

Figure 7. 600 MHz ^{15}N heteronuclear NOE values for SaHPPK in complex with AMPCPP/**3** (red) and AMPCPP/8MG (black). The ^{15}N NOE for the side-chain Hε1 for Trp89 is shown as a large shaded circle. Residues with ^{15}N NOE values less than 0.75 are mapped onto the surface and ribbon representation of the SaHPPK/AMPCPP/**3** X-ray structure. Amides not observed in the ^{15}N HSQC spectra due to severe broadening in loop 3 are colored magenta, and proline residues, cyan.

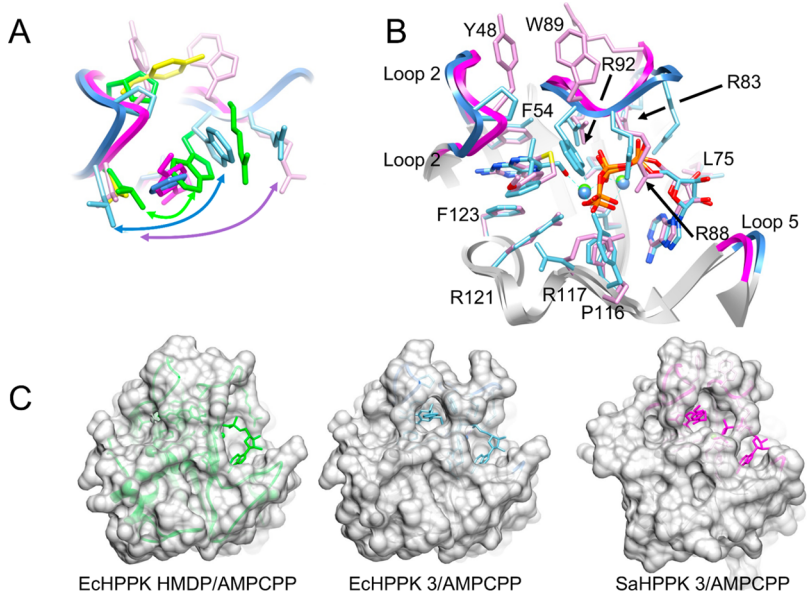

Figure 8. Comparison of the SaHPPK AMPCPP/**3** structure with the EcHPPK/AMPCPP/**2** structure. (A) The substrate pocket in the SaHPPK/AMPCPP/**3** complex (magenta) is more open than that in EcHPPK/AMPCPP/**2** (blue) or in EcHPPK/AMPCPP/HMDP (green), which is completely sealed. (B) Comparison of the active site of SaHPPK/AMPCPP/**3** (magenta) with that of EcHPPK/AMPCPP/**2** (blue). (C) Surface representation of the EcHPPK/AMPCPP/HMDP (left), EcHPPK/AMPCPP/**2** (middle), and SaHPPK/AMPCPP/**3** complexes (right).

statistically relevant regions with increased mobility compared to the global average (0.81). Residues 1 and 158 at the termini are highly mobile (^{15}N NOE < 0.5). A characteristic dip in the ^{15}N NOE values from the global average for amides 47−51 is indicative of some residual fast-time scale motion centered around the interface of loops 2 and 3. Other amides experiencing limited motion include Arg92 in the hinge of loop 3 and Glu103, located in a loop leading into the β hairpin, within which Asp107 and Leu111 are also partly mobile.

The data were compared with that for the 8MG/AMPCPP/SaHPPK complex (shown in black) by recording the sample under identical conditions and with the same pulse sequence. A combination of a newer cryoprobe and a more optimal pulse sequence afforded much better water suppression than previously achieved for 8MG/AMPCPP/SaHPPK[21] and yielded very similar results for both ternary complexes, with the standard deviation of the average value noticeably smaller than that reported earlier (0.08 vs 0.12). The ^{15}N NOE for the side chain of Trp89 appears to be essentially the same for both the **3**/AMPCPP/SaHPPK and 8MG/AMPCPP/SaHPPK complexes, with a degree of residual fast motion similar to that observed for loop 2, indicating that the interaction of the pendant of **3** with this residue is not strong enough to dampen Trp89's fast time scale motion entirely. From a structural perspective, this observation may be more consistent with the position of the Trp89 side chain observed in the X-ray structure compared to that observed in the HMDP/AMPCPP/EcHPPK ternary complex.[40]

dx.doi.org/10.1021/jm501417f | J. Med. Chem. XXXX, XXX, XXX−XXX

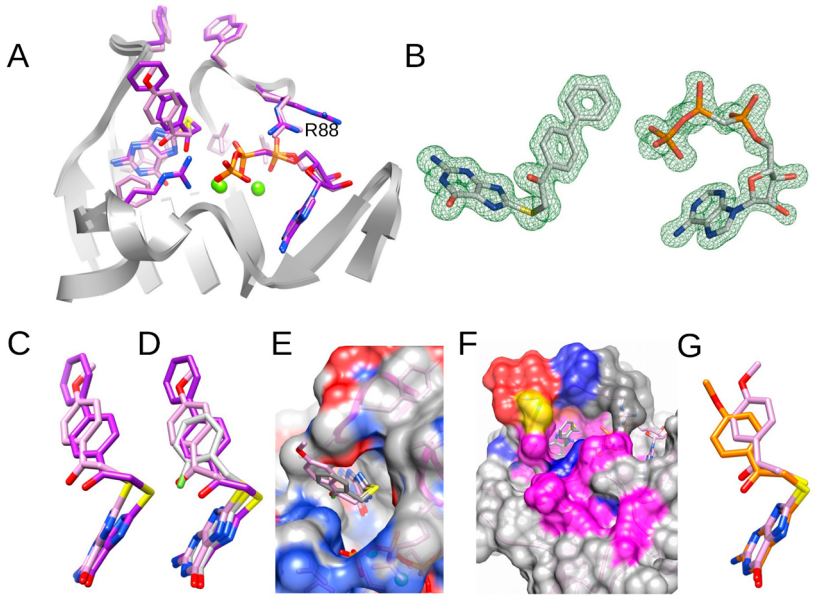

Figure 9. (A) Overview of the active sites of the SaHPPK/AMPCPP/**3** (pink) with SaHPPK/AMPCPP/**7** complexes and (B) the mF_o − DF_c difference density map of the ligands in the SaHPPK/AMPCPP/**7** complex contoured at 3.0σ. (C) Superposition of the bound poses for **3** (pink) and **7** (magenta) with (D) the modeled bound pose of **11** (white). (E) **3** and **11** shown within a surface representation of the substrate pocket. (F) Raw CSPs corresponding to the change in the weighted average chemical shifts observed for **11**/AMPCPP/SaHPPK relative to 8MG/AMPCPP/SaHPPK in the 2D ^{15}N HSQC NMR spectra, mapped onto the docked **11**/AMPCPP/SaHPPK structure. The CSPs are colored pink, blue, and red for those greater than the 1, 2, or 3 times the standard deviation of the CSP values shown in Figure 3C. The broadened Gly47 is colored yellow. (G) The bound pose of **3** in the EcHPPK/AMPCPP/**3** (PDB: 4M5J, orange) is different from that in the SaHPPK/AMPCPP/**3** structure (pink).

Even though **3** is larger than 8MG, binds more tightly to the AMPCPP/SaHPPK complex (by over an order of magnitude), and protrudes into the loop 2/3 region, amide signals for residues 84−89 in loop 3 were not observed in the NMR spectra of **3**/AMPCPP/SaHPPK (magenta in Figure 7), revealing large amplitude motion on the slower (micro- to millisecond) time scale. Thus, the addition of the pendant to the 8MG parent scaffold appears to have limited large-scale impact on the overall micro- to millisecond backbone dynamics of loop 3. However, given that the pendant forms few intermolecular interactions with side-chain atoms, this is not entirely unexpected.

Comparison of the Structures of 3/AMPCPP/SaHPPK, 2/AMPCPP/EcHPPK, and 3/AMPCPP/EcHPPK. Given the broad similarity in the structures of inhibitors **2** and **3** and the sequence similarity between EcHPPK and SaHPPK, it is not surprising that the **3**/AMPCPP/SaHPPK structure is generally quite similar to that of the previously reported **2**/AMPCPP/EcHPPK ternary complex (PDB: 1DY3) (Figure 8A,B),[34] with the cofactor loop 3 closed in over the active site in both cases, compared with the extended conformation observed in the 8MG/SaHPPK binary complex.[21]

In the case of the *E. coli* enzyme, a comparison of the **2**/AMPCPP/EcHPPK complex with the substrate/AMPCPP/EcHPPK complex[40] shows that the binding of **2** leads to an opening of the substrate pocket lid, revealing a solvent-exposed active site pocket, filled by the phenethyl pendant of **2**. This widening to accommodate **2** causes a rotation and 3.6 Å positional change in the side-chain methyl groups of Leu45 and a 3.1 Å sized hinge movement of Trp89 (Figure 8A). Although the equivalent SaHPPK structure in complex with HMDP and AMPCPP has not been crystallized, a comparison with the 8MG structure[21] reveals that the rotation of the equivalent Val46 methyl groups is significantly smaller (<1 Å) in comparison (Figure 8A).

Although the phenyl rings of **2** and **3** in the enzyme complexes occupy similar positions, the position of the side chain of the Trp89 residue is markedly different in the two structures (Figure 8B). In the **2**/AMPCPP/EcHPPK structure, the Trp89 indole ring orients toward the binding site, forming an edge-on π-stacking interaction with the phenyl ring of **2** on one side and the Arg88 residue on the other, and the indole ring Hε2 atom makes a hydrogen-bond contact to the γ-phosphate of ATP. In the SaHPPK structure, however, Trp89 orients away from the binding site to form a hydrophobic contact with the loop 2 residue, Tyr48 (Pro in EcHPPK). The Arg88 guanidinium group is translated 5 Å deeper into the cofactor site, where it appears to hydrogen bond to the heterocyclic ribose oxygen of AMPCPP.

For EcHPPK, formation of the HMDP/AMPCPP ternary complex involves a hydrogen-bond network that depends on the interaction of residues Asn11 and Gln51 (equivalent to Asn10 and Gln50 in SaHPPK) to draw all three loop regions into the fleeting transition state conformation.[23] While we have not yet solved the structure of the HMDP/AMPCPP/SaHPPK complex, it is possible that a Trp89-Tyr48 interaction helps to stabilize the interaction between loops 2 and 3 within this complex. A surface representation of all three ternary complexes (Figure 8C) illustrates that the positioning of the Trp89 and Arg88 residues in the **3**/AMPCPP/SaHPPK complex leads to a larger, more solvent-accessible binding pocket than that in the **2**/AMPCPP/EcHPPK complex. In contrast, the substrate-binding site is completely shielded from solvent in the HMDP/AMPCPP/EcHPPK complex.[40]

Comparing the cofactor sites, in EcHPPK, three arginines (Arg82, Arg84, and Arg92) bind the phosphates of AMPCPP in **2**/AMPCPP/EcHPPK. For SaHPPK, Arg83 and Arg92 replace the roles of Arg84 and Arg92 in EcHPPK; however, Arg85 points in the opposite direction to the equivalent Arg84 in EcHPPK (Figure 8B). This difference may be due to the single-residue

dx.doi.org/10.1021/jm501417f | J. Med. Chem. XXXX, XXX, XXX−XXX

Table 2. SAR for Compounds 3−13

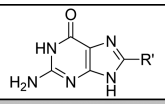

Compound	R'	SaHPPK[a] K_D (μM)	SaHPPK[b] K_D (μM)	EcDHPS[b] K_D (μM)
8MG	SH	12.6 ± 1.3	10.8 ± 0.4[c]	76.2 ± 12
3	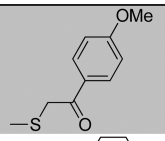	1.1 ± 0.1	76.6 ± 17	3.9 ± 0.2
4	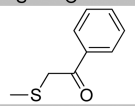	1.4 ± 0.2	10.3 ± 3.6	3.9 ± 0.7
5	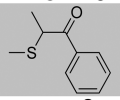	1.9 ± 0.7	7.5 ± 0.1	8.2 ± 2.4
6	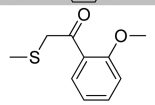	2.8 ± 0.4	21.7 ± 3.8	1.6 ± 0.5
7	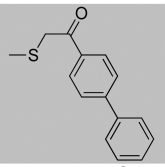	0.81 ± 0.01	21.5 ± 1.1	8.4 ± 1.3
8	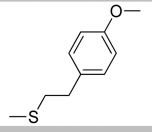	7.8 ± 0.50	73.5 ± 6.40	14.2 ± 0.40
9	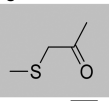	1.85 ± 0.07	42.7 ± 11.2	7.8 ± 1.0
10	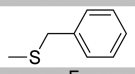	1.79 ± 0.69	13.5 ± 0.21	43.9 ± 9.8
11	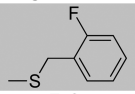	0.45 ± 0.095	4.3 ± 0.6	8.5 ± 2.1
12	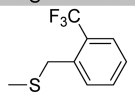	2.81 ± 0.14	7.26 ± 0.12	9.74 ± 0.88
13	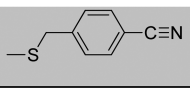	0.66 ± 0.035	11.1 ± 1.3	12.3 ± 0.6

[a]With 1 mM ATP present. [b]No ATP present. [c]Chhabra et al.[21]

insertion in loop L3 in the *E. coli* enzyme (Ala86). Arg84 in EcHPPK hydrogen bonds to the α-phosphate of AMPCPP, resulting in a difference of 1.2 Å in the positioning of the O5′ atoms in the two ternary structures. The position of the O3′ atoms also differs by 2.3 Å, likely due to interaction with Gln74 in EcHPPK and Leu75 in SaHPPK, which alters the ring pucker (C2′ endo in SaHPPK and C3′ endo in EcHPPK). The change in the O2′ positions in the two puckers and the hydrogen bond from O2′ to the backbone of Lys110 in SaHPPK (Arg110 in EcHPPK) may explain the observed 2.5 Å difference in the positioning of the tip of the cofactor loop 5 (Figure 8B).

During the later stages of this work, Yun et al.[41] also reported the X-ray structure of **3** in complex with AMPCPP/EcHPPK. A comparison of the **3**/AMPCPP/SaHPPK and **3**/AMPCPP/EcHPPK structures reveals some interesting differences pertaining to the active site region. Most notably, the active site is more solvent-exposed in the SaHPPK structure, and the pendant of **3** adopts different poses, with the ketone oxygen and para carbon of the pendant ring differing in position by 1.6 and 1.2 Å, respectively, between the two structures (Figure 9F). Given that the NMR data for the **3**/AMPCPP/SaHPPK complex indicates that both residues are in close contact with the ligand and that the loops surrounding the pendant of **3** are not completely rigidified on either the fast or slow time scale, it would be interesting to conduct a similar study on **3**/AMPCPP/EcHPPK.

SAR of Compound 3 and Other S8-Substituted Guanine Analogues. To probe the contribution of specific

dx.doi.org/10.1021/jm501417f | J. Med. Chem. XXXX, XXX, XXX−XXX

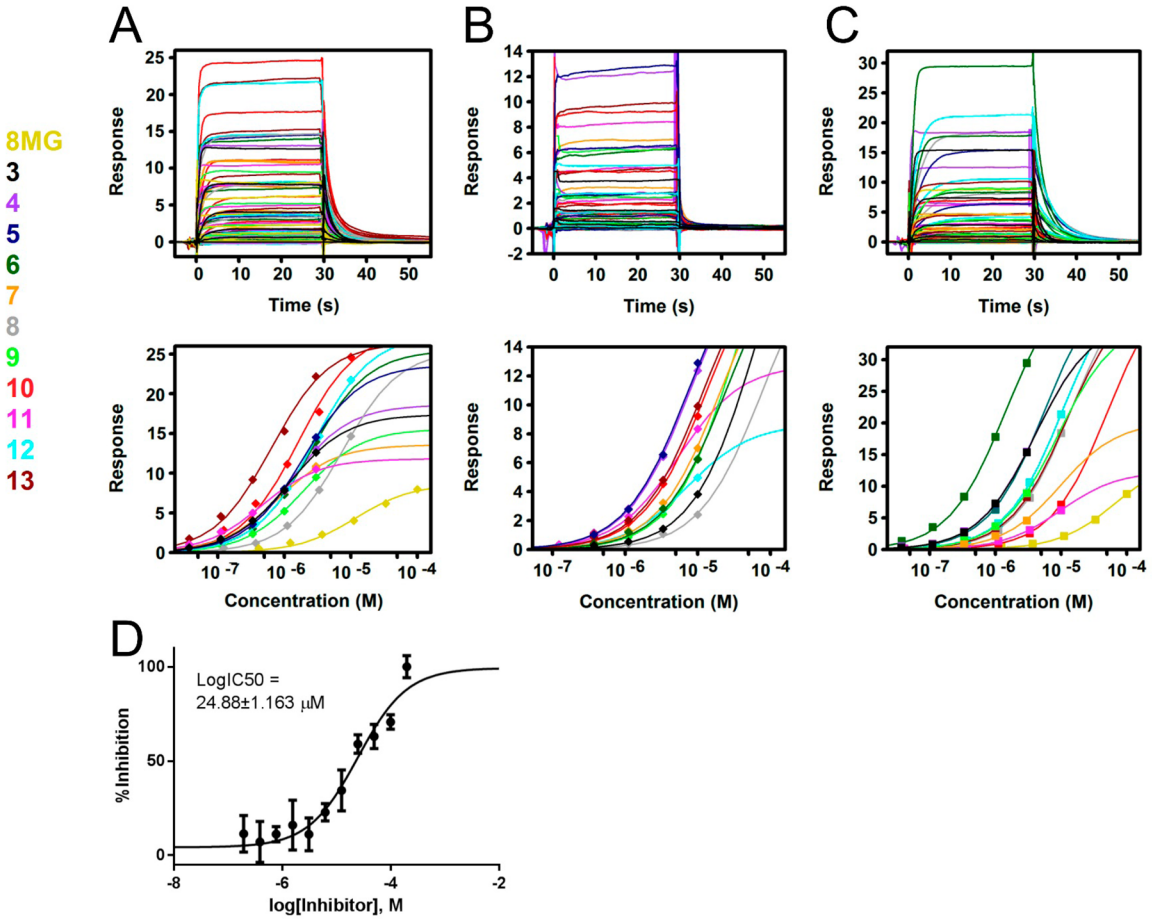

Figure 10. SPR sensorgrams (top panels) and steady-state affinity fits (middle panels) for the binding of all compounds to SaHPPK in the (A) presence or (B) absence of 1 mM ATP and to (C) EcDHPS. (D) Kinase-Glo assay results for compound **11**. Error bars indicate SEM.

groups to the binding affinity of **3** toward SaHPPK, we embarked on a SAR investigation and synthesized a series of S8-substituted 8MG analogues. The affinity and activities for the series of compounds are shown in Table 2 and Figure 10.

We first investigated the likely contributions of the methylene, aryl, carbonyl and methoxy groups of **3** (K_D = 1.1 μM) toward its affinity for the cofactor-bound enzyme. Removal of the 4-methoxy (compound **4**, K_D = 1.4 μM) had little effect on binding, an observation predicted from the solvent-exposed nature of this group in the X-ray structure (Figure 3A). A branched methylene was also tolerated (**5**), furnishing a K_D = 1.8 μM, whereas moving the 4-methoxy group to the 2-position (**6**) gave a slight loss of affinity (K_D = 2.8 μM). Furthermore, replacement of the 4-methoxy group with a phenyl group to give biphenyl **7** did not significantly alter affinity (K_D = 0.81 μM). Saturation of the ketone group to give the methylene analogue **8**, on the other hand, led to a significant decrease in affinity (K_D = 7.8 μM), which is again supported by the structural data, which revealed a specific interaction between the ketone group and the side chain of Arg121 in **3**. Replacement of the aryl ring with a methyl group (**9**) led to only a slight decrease in affinity (K_D = 1.9 μM), suggesting that the interactions of the aryl ring with the enzyme are not strong, consistent with the relatively open or dynamic nature of the active site around the aryl group.

In their recent study with EcHPPK, Yun et al.[41] also found that the 4-OMe group in **3** was not important for binding to EcHPPK. However, in contrast to our findings for SaHPPK, they found that a branched methylene linker and moving the 4-methoxy to the 2-position (**6**) led to complete abrogation of activity, which is again suggestive of a more open active site around the aryl group in SaHPPK. Furthermore, they found that large groups at the 4-position were not tolerated, whereas we have shown that they can be for SaHPPK. Indeed, we were able to crystallize and solve the structure of the biphenyl analogue **7** in complex with AMPCPP (Figure 9A,B). The structure is remarkably similar to that of the **3**/AMPCPP/SaHPPK complex. The largest differences are found in the orientation of the Arg88 side chain, which is split between two conformations. The difference of most relevance to the SAR analysis, however, is the change in the position of the ketone group (2.2 Å), which maintains the stacking between the Arg121 guanidinium group and the sulfur atom (Figure 8A,C). The position of the sulfur in the biphenyl analogue is essentially the same as that in the 8MG/SaHPPK binary structure.

In view of the observed changes in the sulfur and carbonyl positions (Figure 9C) in the cofactor-bound SaHPPK complexes of **3** and **7**, it was reasoned that removal of a carbon from the linker in **3** might serve to draw the aryl ring down into the position observed in the **7**/AMPCPP/SaHPPK structure. We reasoned that π stacking would be possible via the phenyl ring tethered to a shortened linker and that this could replace the ketone π system. Synthetic efforts were thus directed toward shortening the linker in **3** to a substituted benzyl group. Listed in Table 2 are the results for the unsubstituted compound **10**, which effectively represents a direct replacement of the acetyl group of **9** with a phenyl ring. Gratifyingly, activity was maintained (K_D = 1.8 μM). A limited set of analogues was then assembled, the most

dx.doi.org/10.1021/jm501417f | J. Med. Chem. XXXX, XXX, XXX−XXX

interesting of which are shown in Table 2. Here, it can be seen that a 2-CF_3 group results in a relative loss of affinity (**12**, K_D = 2.8 μM). However, the 2-fluorobenzyl analogue **11** displayed an increase in affinity toward SaHPPK, with a K_D of 453 nM. Another compound of interest was the 4-cyano analogue **13**, which also displayed strong affinity toward SaHPPK with a K_D of 660 nM. Compared with **3**, compounds **11** and **13** benefit from a reduced molecular weight and number of rotatable bonds. For these reasons, in addition to the comparative ease of synthesis of these and other S-benzyl-substituted compounds, compounds such as **11** and **13** represent promising leads for further development. Interestingly, **11** also binds appreciably to the apo enzyme and does so to a far greater extent than that of **3**, with respective K_D values of 4.3 and 77 μM. It may therefore be a good synthetic starting point for investigating cofactor-competitive binders or moieties that bind at the metal site, perhaps by combining SAR from our previously reported cofactor-competitive N7 ethyl alcohol 8MG analogue (K_D = 10 μM for the apo enzyme).[20] Compound **13** also corresponds to the only S-benzyl-substituted analogue of 8MG tested by Yun et al.[41] In contrast to our findings for SaHPPK, this compound exhibits very poor affinity for EcHPPK.

Crystallization attempts with **11** were unsuccessful; therefore, docking of **11** into the SaHPPK crystal structure was undertaken (Figure 9D, E). The resulting model suggests that the fluorine atom could position itself relative to the guanidinium group in a manner similar to that of the ketone group in **3**. This could plausibly confer increased affinity, as the guanidinium group is known to be highly fluorophilic and can interact strongly with a negatively polarized fluorine, favoring parallel orientations to the guanidinium plane,[42] as observed in the docked model. The model indicates that the phenyl ring can overlay with the first ring in the biphenyl analogue **7**, maintaining interactions to Val46. A reason for the lower binding affinity of **12** could be due to the likely propensity for the 2-CF_3 group to twist the phenyl ring out of plane. The ^{15}N HSQC spectrum of **11**/AMPCPP/SaHPPK was assigned using the HNCA experiment, as was done for the spectrum of **3**/AMPCPP/SaHPPK. Comparing the differential CSPs of 8MG/AMPCPP-saturated SaHPPK with either **3**/AMPCPP/SaHPPK (Figure 3C) or **11**/AMPCPP/SaHPPK (Figure 9F and Supporting Information Figure S1) reveals very similar pattern of CSPs but with notably larger differential CSPs for Tyr48 and Glu50 amides in loop 2. Of note, the signal for Gly47, the nearest amide to the pendant of **11** in the model, was not observed in the spectra (shown in yellow in Figure 9F) but was in the complex with **3**, most likely due to subtle motional effects of the proximal phenyl ring of the pendant on a micro- to millisecond time scale. The larger differential CSPs (>3σ) of Tyr48 and Glu50 (shown in red) may represent a conformational change in loop 2, which also effects the stacking interaction with Trp89, as evidenced by differential CSPs of >2σ (shown in blue). Substantial differences were also noted in the arginine side-chain region of the spectra (data not shown), which may be consistent with the Arg121 guanidinium−fluorine interaction predicted by the model. Although the observed NMR chemical shift data is supportive of the docked pose of **11**, assignment of the NMR signals of the side-chain atoms will be a prerequisite to determine the precise bound structure of **11**.

The binding data for **13**, **6**, and **7** highlights a clearly divergent SAR trend for SaHPPK and EcHPPK. The higher affinity of the latter two compounds for SaHPPK can be reconciled on the basis of the observed increased size/plasticity of the binding pocket for SaHPPK. In the case of **13**, the para-attached cyano group polarizes the aryl ring, which would favor the π interaction with the Arg121, presumably for both enzymes. It is unclear why this would decrease the affinity compared to that of **3** for the EcHPPK enzyme. The enhanced affinity for SaHPPK may have its origins in the different pendant poses for **3** bound to the two enzymes (Figure 9G) as well as differences in the orientation of the methyl groups of Leu45 in EcHPPK and Val46 in SaHPPK (Figure 8A). In order to assess whether enhanced affinity translated into enhanced functional inhibition of HPPK, we selected **11** and tested it alongside 8MG (IC_{50} = 41 μM)[20,21] to obtain the IC_{50} value. This gave rise to a value of 25 μM (Figure 10), suggesting that, while the higher affinity of **11** for HPPK gives rise to increased functional inhibition, the increase is not as great as might have been expected in view of **11**'s much higher affinity for HPPK (in the presence of ATP). However, it is noted that in terms of drug-likeness, our lead compound **11** has a number of favorable properties. For a compound with submicromolar affinity, it has a relatively low molecular weight of 291 Da, a topological polar surface area (tPSA) of 95 Å^2, suitable for membrane permeability and oral availability,[43] and a cLogP of 3.5. On the downside, it contains four hydrogen-bond donors, and, accordingly, its membrane penetration ability was found to be poor (A−B $P_{app} = 0.6 \pm 0.2 \times 10^{-6}$ cm s^{-1} for Caco-2 monolayers).

Binding of Compounds to DHPS. Given the chemical similarity of the guanine and pterin scaffolds, the fact that the pterin core is common to both HPPK and DHPS substrates, and that 8MG is a known DHPS binder,[9] it was decided to measure the binding of our 8MG analogues to DHPS from *E. coli* (Figure 10). SPR data showed that compounds **3** and **4** bind DHPS with a K_D of ∼4.0 μM. Furthermore, the best HPPK binder, compound **11**, also binds DHPS with appreciable affinity (K_D ∼ 8.0 μM). These K_D values are notably better than that of 8MG (76.1 μM). As for HPPK binding, the para OMe group in compound **3** was found to have little impact on DHPS binding affinity, and fluorine substitution at the ortho position of the benzyl group appears to be beneficial.

CONCLUSIONS

Building on our previous structure-based approaches toward inhibiting HPPK, we have used a combination of biophysical methods, including SPR, NMR spectroscopy, and X-ray crystallography, to reveal mechanistically important structural changes accompanying binding of a series of 8MG-derived substrate-site inhibitors to cofactor analogue-bound HPPK. In combination with chemical synthesis, this has resulted in the development of an advanced new lead compound (**11**) displaying an affinity for SaHPPK over 20 times greater than the previously reported parent compound, 8MG. Active site structural details for the complexes presented here will assist in the design and development of species-selective or broad-spectrum inhibitors of HPPK. In this regard, it is notable that the binding of 8MG and other analogues to EcHPPK is apparently much weaker than that to SaHPPK.[41] Sequence-related structural differences, discussed here, may present avenues to increased selectivity and potency. A number of the 8MG analogues exhibit appreciable affinity for DHPS, highlighting the potential for this class of compound to be developed into dual-target inhibitors. A major focus of our future work will be on developing analogues of **11** that are able to permeate bacterial membranes, with the goal of achieving antibacterial activity.

dx.doi.org/10.1021/jm501417f | J. Med. Chem. XXXX, XXX, XXX−XXX

EXPERIMENTAL SECTION

Samples of SaHPPK for NMR Spectroscopy. Isotopically labeled protein samples for NMR spectroscopy were prepared as described previously.[21] *E. coli* BL21 (DE3) cells were transformed and grown overnight in 3 mL of 2× YT medium supplemented with 100 μg mL^{-1} kanamycin for selection. The overnight culture was subcultured into 50 mL of minimal media that was grown to an OD_{600} of 0.5−0.7. This was then added to 1 L of minimal media supplemented with 1.5 g of ^{15}N ammonium chloride and/or 3 g of ^{13}C glucose and grown at 310 K until the OD_{600} was 0.5−0.8. Isopropyl β-D-1-thiogalactopyranoside (IPTG) was added to a final optimized concentration of 0.5 mM, and expression was carried out at 293 K for 12 h. Purification was carried out as reported previously.[44]

Preparation of DHPS from *E. coli*. A pET28a plasmid containing the synthesized EcDHPS sequence (Geneart) was cloned with an N-terminal hexahistidine tag and a thrombin cleavage site. *E. coli* BL21 (DE3) cells transformed with the plasmid were grown overnight in 20 mL 2× YT media supplemented with 50 μg mL^{-1} kanamycin for selection. The overnight culture was then subcultured into fresh 2× YT (0.5L) with growth at 310 K for ∼2 h until an OD_{600} of 0.5−0.7 was reached. IPTG was added to a final concentration of 0.3 mM, with expression occurring at 301 K for 22 h. The cultures were centrifuged at 5000 rpm for 10 min, and the cells were resuspended in 50 mL 50 mM Tris, pH 8.5, 5% glycerol, 5 mM $MgCl_2$. An EDTA-free complete protease-inhibitor cocktail tablet (Roche) was added together with lysozyme and DNase to a final concentration of 0.4 and 0.6 mg mL^{-1}, respectively. After 10 min, the cells were sonicated, and the cell debris was removed by centrifugation at 18 000 rpm at 277 K for 30 min. The supernatant was filtered (0.45 μm filter) and loaded onto a Ni-NTA IMAC column (Qiagen). Unbound protein was washed off with 10 mM imidazole in 50 mM Tris buffer, pH 8.5, 0.1 M NaCl, 5% glycerol, 2 mM $MgCl_2$, 1 mM DTT. Protein was eluted from the column with a 500 mM imidazole, DTT-free variant of the above buffer. The protein was further purified using a Superdex 75 size-exclusion 16/60 column (GE Healthcare) and eluted with 50 mM Tris, pH 8.5, 2 mM $MgCl_2$, 2 mM DTT, followed by the use of a MonoQ ion-exchange 16/10 column (GE Healthcare). The column was equilibrated with 50 mM Tris, pH 8.5, 2 mM $MgCl_2$, 2 mM DTT, with elution of protein using an equivalent buffer with the addition of 0.25 M NaCl. Fractions were analyzed using a 15% SDS-PAGE gel with Coomassie staining. Protein was pooled and concentrated to 2 mg mL^{-1} using a 3 kDa molecular weight cutoff ultrafiltration centrifugal device (Amicon). All samples were snap-frozen and stored at 193 K.

NMR Spectroscopy. All NMR experiments were recorded at 295 K on a Bruker Avance 600 MHz NMR spectrometer equipped with a cryoprobe and *Z*-axis gradient. Triple-resonance NMR experiments were performed on a sample of ∼0.25 mM $^{15}N/^{13}C$-labeled SaHPPK dissolved in a 90%/10% H_2O/D_2O HEPES buffer, 1% sorbitol, and 2% DMSO-d_6 at pH 8.0 in the presence of 10 mM $MgCl_2$ and saturating amounts of AMPCPP (0.5 mM). Titrations of compound **3** or **11** to saturation was performed from a 50 mM stock dissolved in DMSO-d_6. Backbone assignments were obtained using the HNCA and HN(CO)-CA experiments, and assignments were further confirmed using a 3D ^{15}N-edited NOESY experiment recorded with a mixing time of 120 ms. 3D experiments used a WATERGATE sequence for solvent suppression. ^{15}N heteronuclear NOE spectra were recorded on a ∼0.36 mM ^{15}N-labeled sample of SaHPPK in the presence of 1 mM AMPCPP and either 600 μM 8MG or ∼400 μM **3** using gradients for coherence selection and sensitivity enhancement. Three seconds of saturation was applied using a binomial train of pulses separated by a delay of 5 ms to generate the desired heteronuclear NOE and was applied off- and on-resonance in an interleaved manner, in addition to 1 s of relaxation delay. Errors were calculated from the baseplane noise level. Spectra were processed using NMRPipe[45] and analyzed with XEASY[46] or SPARKY.[47] 2D ^{15}N HSQC and ^{15}N NOE experiments were typically acquired with t_{1max} (^{15}N) = 51−62 ms and t_{2max} (^{1}H) = 142 ms, whereas triple-resonance experiments were acquired with t_{1max} (^{15}N) = 23.3 ms, t_{2max} (^{13}C) = 10.4 ms, t_{2max} (^{1}H) = 15.1 ms, and t_{3max} (^{1}H) = 142 ms.

Crystallization and X-ray Structure Determination. Crystallization experiments were performed as described previously.[44] In brief, co-crystallization was set up in the C3 screens (CSIRO) at 281 K using sitting-drop vapor-diffusion method with droplets consisting of 150 nL of protein solution and 150 nL of reservoir solution and using a reservoir volume of 50 μL. Crystals of the SaHPPK in complex with AMPCPP were obtained from a solution containing 120 mM magnesium acetate, 12.6% (w/v) PEG 8000, 120 mM Tris, pH 8.5, 1 mM AMPCPP, and the protein at a concentration of 6.9 mg mL^{-1}. Crystals of the **3**/AMPCPP/SaHPPK complex grew from a solution containing 275 mM ammonium nitrate and 22.1% PEG 4000 with a protein concentration of 7.5 mg mL^{-1}. Crystals of the **7**/AMPCPP/SaHPPK complex were grown under similar conditions: 210 mM ammonium nitrate, 22.2% PEG 3350, and a protein concentration of 6.9 mg mL^{-1}. Data were collected at the MX-2 beamline of the Australian Synchrotron (see Table 1 for statistics) using an ADSC Quantum 315 detector, with 270 frames obtained with a one-degree oscillation angle for a complete data set. These data were indexed using XDS[48] and scaled using SCALA.[49] The SaHPPK structure (4AD6) was used to solve the initial phases of the binary and ternary complexes by molecular replacement using Phaser.[50] Refinement was performed using REFMAC5,[51] and the electron density maps were visualized in Coot.[52] After several rounds of manual rebuilding, ligands and water molecules were added, and the models further refined to a resolution of 2.7 Å (R_{free} (%) = 24.2; R_{work} (%) = 19.4) for the AMPCPP complex; to a resolution of 2.0 Å (R_{free} (%) = 20.1; R_{work} (%) = 16.1) for the **3**/AMPCPP/SaHPPK ternary complex, and to a resolution of 1.6 Å (R_{free} (%) = 17.8; R_{work} (%) = 16.0) for the **7**/AMPCPP/SaHHPK ternary complex.

The coordinates of SaHPPK in complex with AMPCPP, in complex with **3**/AMPCPP, and in complex with **7**/AMPCPP have been deposited at the Protein Data Bank with accession numbers 4CYU, 4CRJ, and 4CWB, respectively.

Surface Plasmon Resonance (SPR). All SPR experiments were performed using Biacore T200 biosensor (GE Healthcare). Immobilizations were performed in HBS-^{E}P+ running buffer (10 mM HEPES, pH 7.4, 150 mM NaCl, 50 μM EDTA, 0.05% [v/v] Tween-20) at 298 K with a constant flow-rate of 10 μL min^{-1}. SaHPPK and EcDHPS proteins were covalently coupled to the NTA chip (GE Healthcare) surface using a previously described method.[53] Briefly, a single flow cell on the chip surface was sequentially activated by injecting (1) 40 μL of nickel sulfate and (2) 70 uL of a 1:1 mixture of NHS/EDC (*N*-hydroxysuccinimide/*N*-ethyl-*N*′-(3-diethylaminopropyl)carbodiimide). Recombinant protein was diluted in the running buffer (SaHPPK to 225 μg mL^{-1}; EcDHPS to 80 μg mL^{-1}) and injected over an activated flow cell for 20 min (200 μL). Amine-coupled surface was subsequently blocked with 70 μL of 1 M ethanolamine, pH 8.0, and then further regenerated with two 10 μL injections of 350 mM EDTA prepared in running buffer. Using this coupling approach, average immobilization levels achieved were 5400 RU for SaHPPK and 7200 RU for EcDHPS. Additionally, ubiquitin-specific-processing protease 7 (USP7) was coupled in a similar fashion to provide for an unrelated negative control surface (6600 RU). All SPR binding experiments were performed at 293 K in SPR binding buffer (50 mM HEPES, pH 8.0, 150 mM NaCl, 5 mM DTT, 10 mM $MgCl_2$, 0.05% [v/v] Tween-20, 5% [v/v] DMSO). Analytes were serially diluted (3-fold) in SPR binding buffer, injected for 30 s contact time at 60 μL min^{-1}, and then allowed to dissociate for 60 s. Each analyte titration was performed in duplicate or greater. Binding sensorgrams were processed, solvent-corrected, and double-referenced using Scrubber software (BioLogic Software, Australia). SPR binding analysis of several of the compounds investigated in this study revealed dissociation rates that were not sufficiently slow to allow global fitting to a kinetic binding model, for which the k_d (dissociation rate constant) must typically be <0.5 s^{-1} for SPR instruments to be able to capture sufficient data points during the dissociation phase. Therefore, to determine binding affinities (K_D values), responses at equilibrium for each analyte were fitted to a 1:1 steady-state affinity model available within Scrubber using 8MG as a reference, as previously described.[20]

KinaseGlo Biochemical Assay. HPPK activity was quantified using a KinaseGlo assay kit (Promega) as previously reported.[21] In this, firefly luciferase utilizes the remaining ATP after HPPK catalysis, producing a

dx.doi.org/10.1021/jm501417f | J. Med. Chem. XXXX, XXX, XXX−XXX

luminescence signal that is directly proportional to ATP concentration. The enzyme activity and optimum concentration to define kinetic parameters were optimized as described previously.[21] For kinetic measurements, an optimized HPPK concentration of 0.4 ng μL^{-1} assay volume was used, which allowed for monitoring of the first 10% of reaction turnover within a reasonable time period (20 min). Measurements were performed in 96-well plates using assay buffer (100 mM Tris-HCl, pH 8.5, 10 mM $MgCl_2$, 0.01% (w/v) BSA, 0.01% (v/v) Tween 20 and 10 mM β-mercaptoethanol). Typically, 5 μL of test compound (dissolved in 50% DMSO) and 20 μL of enzyme were added to each well followed by 25 μL of assay buffer, giving 0.3 μM pterin and 0.2 μM ATP in a total reaction volume of 50 μL. After 20 min incubation at room temperature, the enzymatic reaction was stopped with 50 μL of KinaseGlo reagent. Luminescence was recorded after a further 10 min using a FLUOstar Optima plate reader (BMG, Labtech Ltd.). Reactions were performed in triplicate. Kinetic data and inhibition data were fit to Michaelis–Menten and sigmoidal dose–response equations, respectively, using GraphPad Prism.

Molecular Modeling. Molecular modeling was performed using the Schrödinger Suite 2014 (www.schrodinger.com) through the Maestro interface (Maestro, version 9.7).[54] Protein preparation of 4CWB was performed with the Protein Preparation Wizard workflow implemented by Schrödinger (Epik, version 2.7),[55] with deletion of all waters. In order to eliminate any bond length or bond angle biases in the structures, compound **11** was subjected to a full minimization prior to docking using LigPrep (LigPrep, version 2.9).[56] Docking was carried out with Glide,[57] version 6.2, using Extra Precision (XP) mode.

Compound Procurement and Analysis. 8MG and compound **3** were purchased from Sigma-Aldrich and TimTec, respectively. All other compounds were synthesized as described below. In all cases, ^{1}H NMR spectra were recorded on a 400 MHz Bruker NMR spectrometer, and chemical shifts were referenced to the solvent peak. Analytical reversed-phase high-performance liquid chromatography (RP-HPLC) was performed on an Agilent 1260 Infinity HPLC system using an Agilent Eclipse Plus C18 column (100 × 4.6 mm i.d., 3.5 μm) with a flow rate of 1 mL min^{-1} and UV detection at 214 and 254 nm. Elution was achieved with standard HPLC buffers (buffer A: 99.9% H_2O/0.1% TFA; buffer B: 99.9% CH_3CN/0.1% TFA) using a gradient from 5% B/95% A to 100% B over 10 min. All compounds were determined to be >95% purity by this method.

General Procedure A for the Synthesis of Compounds 4–7 and 9. 8-Mercaptoguanine (0.200 g, 1.09 mmol) was dissolved in 0.4 M NaOH (5.5 mL), and to the solution was added phenacyl bromide (or analogue) (0.24 g, 1.2 mmol) in ethanol (0.9 mL). The reaction was allowed to stir for 2 h, following which a white precipitate formed in solution, which was collected by vacuum filtration to give the title compound as a white amorphous solid.

2-Amino-8-((2-oxo-2-phenylethyl)thio)-1,9-dihydro-6*H*-purin-6-one (4). Compound **4** was synthesized using general procedure A. Yield 50%. ^{1}H NMR (DMSO-d_6, 400 MHz): δ 12.51 (bs, 1H), 10.90 (bs, 1H), 8.03–8.01 (m, 2H), 7.67 (t, J = 7.4 Hz, 1H), 7.55 (t, J = 7.7 Hz, 2H), 6.45 (s, 2H), 4.86 (s, 2H). HRMS: m/z calcd for $[M + H]^+$ $C_{13}H_{11}N_5O_2S$, 302.0706; found, 302.0710.

2-Amino-8-((1-oxo-1-phenylpropan-2-yl)thio)-1,9-dihydro-6*H*-purin-6-one (5). Compound **5** was synthesized using general procedure A including the following work up. The reaction mixture was diluted with 0.5 M NaOH (7 mL). The aqueous layer was extracted with EtOAc (3 × 3 mL) and acidified with acetic acid (2 mL). The precipitate solid was collected by filtration and dried to give solid product. Yield 28%. ^{1}H NMR (DMSO-d_6, 400 MHz) δ 10.91 (bs, 1H), 8.01 (d, J = 7.4 Hz, 2H), 7.65 (t, J = 7.3 Hz, 1H), 7.52 (t, J = 7.7 Hz, 2H), 6.46 (bs, 2H), 5.43 (q, J = 6.7 Hz, 1H), 1.53 (d, J = 6.9 Hz, 3H). HRMS: m/z calcd for $[M + Na]^+$ $C_{14}H_{13}N_5O_2S$, 338.0682; found, 338.0688.

2-Amino-8-((2-(2-methoxyphenyl)-2-oxoethyl)thio)-1,9-dihydro-6*H*-purin-6-one (6). Compound **6** was synthesized using general procedure A including the following work up. The reaction mixture was diluted with 0.5 M NaOH (7 mL). The aqueous layer was extracted with EtOAc (3 × 3 mL) and acidified with acetic acid (2 mL). The precipitate solid was collected by filtration and dried to give solid product. Yield 63%. ^{1}H NMR (DMSO-d_6, 400 MHz) δ 10.58 (bs, 1H), 7.64 (dd, J = 7.7, 1.8 Hz, 1H), 7.59 (m, 1H), 7.21 (d, J = 8.3 Hz, 1H), 7.08–7.01 (m, 1H), 6.28 (bs, 2H), 4.67 (s, 2H), 3.92 (s, 3H). HRMS: m/z calcd for $[M + H]^+$ $C_{14}H_{13}N_5O_3S$, 332.0812; found, 332.0821.

8-((2-([1,1′-Biphenyl]-4-yl)-2-oxoethyl)thio)-2-amino-1,9-dihydro-6*H*-purin-6-one (7). Compound **7** was synthesized using general procedure A. Yield 9%. ^{1}H NMR (DMSO-d_6, 400 MHz): δ 10.97 (s, 1H), 8.11 (d, J = 8.5 Hz, 2H), 7.82 (d, J = 8.5 Hz, 2H), 7.77–7.74 (m, 2H), 7.50 (m, 2H), 7.45–7.43 (m, 1H), 6.39 (s, 2H), 4.80 (s, 2H). HRMS: m/z calcd for $[M + H]^+$ $C_{19}H_{15}N_5O_2S$, 378.1019; found, 378.1028.

2-Amino-8-((2-oxopropyl)thio)-1,9-dihydro-6*H*-purin-6-one (9). Compound **9** was synthesized using general procedure A using 4 equiv of chloroacetone and 8 mL of 0.4 M NaOH. Yield 55%. ^{1}H NMR (DMSO-d_6, 400 MHz): δ 12.60 (bs, 1H), 10.65 (bs, 1H), 6.33 (s, 2H), 4.16 (s, 2H), 2.23 (s, 3H). HRMS: m/z calcd for $[M + H]^+$ $C_8H_9N_5O_2S$, 240.0550; found, 240.0553.

General Procedure B for the Synthesis of Compounds 8 and 10–13. 8-Mercaptoguanine (0.10 g, 0.55 mmol) was dissolved in 0.5 M NaOH (3 mL), and to the solution was added substituted benzyl or phenethyl bromide (0.61 mmol). The mixture was stirred at room temperature for 5–24 h and then diluted with 0.5 M NaOH (8 mL). The aqueous layer was extracted with EtOAc (3 × 20 mL), acidified with acetic acid (pH 5.0), and stirred for 15–20 min. The precipitated solid was collected by filtration, washed thoroughly with water and ethanol, and dried to give the solid product.

2-Amino-8-((4-methoxyphenethyl)thio)-1,9-dihydro-6*H*-purin-6-one (8). Compound **8** was synthesized using general procedure B. Yield 73%. ^{1}H NMR (DMSO-d_6, 400 MHz) δ: 12.5 (bs, 1H), 10.5 (bs, 1H), 7.18–6.84 (m, 4H), 6.55 (s, 2H), 3.72 (s, 3H), 3.33 (t, J = 7.7 Hz, 2H,), 2.88 (t, J = 7.1 Hz).HRMS: m/z calcd for $[M + H]^+$ $C_{14}H_{15}F_3N_5O_2S$, 318.1019; found, 318.1021.

2-Amino-8-(benzylthio)-1,9-dihydro-6*H*-purin-6-one (10). Compound **10** was synthesized using general procedure B. Yield 36%. ^{1}H NMR (DMSO-d_6, 400 MHz) δ: 12.5 (bs, 1H, NH), 10.5 (bs, 1H), 7.29–7.21 (m, 5H), 6.57 (s, 2H), 4.34 (s, 2H). HRMS: m/z calcd for $[M + H]^+$ $C_{12}H_{11}N_5OS$, 274.0757; found, 274.0760.

2-Amino-8-((2-fluorobenzyl)thio)-1,9-dihydro-6*H*-purin-6-one (11). Compound **11** was synthesized using general procedure B. Yield 66%. ^{1}H NMR (DMSO-d_6, 400 MHz) δ: 12.5 (bs, 1H), 10.5 (bs, 1H), 7.37–7.03 (m, 4H), 6.30 (s, 2H), 4.30 (s, 2H). HRMS: m/z calcd for $[M + H]^+$ $C_{12}H_{10}FN_5OS$, 292.0663; found, 292.0666.

2-Amino-8-((2-(trifluoromethyl)benzyl)thio)-1,9-dihydro-6*H*-purin-6-one (12). Compound **12** was synthesized using general procedure B. Yield 52%. ^{1}H NMR (DMSO-d_6, 400 MHz) δ: 12.6 (bs, 1H), 10.6 (bs, 1H), 7.75–7.48 (m, 4H), 6.36 (s, 2H), 4.53 (s, 2H). HRMS: m/z calcd for $[M + H]^+$ $C_{13}H_{10}F_3N_5OS$, 342.0631; found, 342.0636.

4-(((2-Amino-6-oxo-6,9-dihydro-1*H*-purin-8-yl)thio)methyl)-benzonitrile (13). Compound **13** was synthesized using general procedure B. Yield 73%. ^{1}H NMR (DMSO-d_6, 400 MHz) δ 10.89 (bs, 1H), 7.77 (d, J = 8.3 Hz, 2H), 7.55 (d, J = 8.3 Hz, 2H), 6.43 (bs, 2H), 4.45 (s, 2H). HRMS: m/z calcd for $[M + H]^+$ $C_{13}H_{10}N_6OS$, 299.0710; found, 299.0699.

■ ASSOCIATED CONTENT

Ⓢ Supporting Information

CSP data for the binding of **11** to AMPCPP saturated SaHPPK. This material is available free of charge via the Internet at http://pubs.acs.org.

Accession Codes

The coordinates of SaHPPK in complex with AMPCPP, in complex with **3**/AMPCPP, and in complex with **7**/AMPCPP have been deposited at the Protein Data Bank with accession numbers 4CYU, 4CRJ, and 4CWB, respectively.

■ AUTHOR INFORMATION

Corresponding Author

*Tel.: ++61 3 9903 9543. E-mail: james.swarbrick@monash.edu.

Notes

The authors declare no competing financial interest.

■ ACKNOWLEDGMENTS

All SaHPPK crystals were grown at the C3 Crystallization Centre at CSIRO, Parkville, Australia, and X-ray data were obtained at the MX2 beamline at the Australian Synchrotron, Victoria, Australia. We thank OpenEye for a license to use their software. J.B.B. was supported by an NHMRC Research Fellowship (1020411).

■ ABBREVIATIONS USED

HMDP, 6-hydroxymethyl-7,8-dihydro-pterin; SMX, sulfamethoxazole; TMP, trimethoprim; SaHPPK, 6-hydroxymethyl-7,8-dihydropterin pyrophosphokinase from *S. aureus*; EcHPPK, 6-hydroxymethyl-7,8-dihydropterin pyrophosphokinase from *E. coli*; EcDHPS, dihydropteroate synthase from *E. coli*; MRSA, methicillin-resistant *S. aureus*; 8MG, 8-mercaptoguanine; SPR, surface plasmon resonance; HSQC, heteronuclear single quantum coherence; SAR, structure−activity relationships

■ REFERENCES

(1) Bermingham, A.; Derrick, J. P. The folic acid biosynthesis pathway in bacteria: evaluation of potential for antibacterial drug discovery. *BioEssays* **2002**, *24*, 637−648.

(2) Swarbrick, J. D.; Iliades, P.; Simpson, J. S.; Macreadie, I. Folate biosynthesis - reappraisal of old and novel targets in the search for new antimicrobials. *Open Enzyme Inhib. J.* **2008**, *1*, 12−33.

(3) Masters, P. A.; O'Bryan, T. A.; Zurlo, J.; Miller, D. Q.; Joshi, N. Trimethoprim-sulfamethoxazole revisited. *Arch. Int. Med.* **2003**, *163*, 402−410.

(4) Adra, M.; Lawrence, K. R. Trimethoprim/sulfamethoxazole for treatment of severe *Staphylococcus aureus* infections. *Ann. Pharmacother.* **2004**, *38*, 338−341.

(5) Forgacs, P.; Wengenack, N. L.; Hall, L.; Zimmerman, S. K.; Silverman, M. L.; Roberts, G. D. Tuberculosis and trimethoprim-sulfamethoxazole. *Antimicrob. Agents Chemother.* **2009**, *53*, 4789−4793.

(6) Martin, S. I.; Fishman, J. A. *Pneumocystis pneumonia* in solid organ transplant recipients. *Am. J. Transplant.* **2009**, *9*, S227−S233.

(7) Pashley, T. V.; Volpe, F.; Pudney, M.; Hyde, J. E.; Sims, P. F.; Delves, C. J. Isolation and molecular characterization of the bifunctional hydroxymethyldihydropterin pyrophosphokinase-dihydropteroate synthase gene from *Toxoplasma gondii*. *Mol. Biochem. Parasitol.* **1997**, *86*, 37−47.

(8) Thera, M. A.; Sehdev, P. S.; Coulibaly, D.; Traore, K.; Garba, M. N.; Cissoko, Y.; Kone, A.; Guindo, A.; Dicko, A.; Beavogui, A. H.; Djimde, A. A.; Lyke, K. E.; Diallo, D. A.; Doumbo, O. K.; Plowe, C. V. Impact of trimethoprim-sulfamethoxazole prophylaxis on falciparum malaria infection and disease. *J. Infect. Dis.* **2005**, *192*, 1823−1829.

(9) Hevener, K. E.; Yun, M. K.; Qi, J.; Kerr, I. D.; Babaoglu, K.; Hurdle, J. G.; Balakrishna, K.; White, S. W.; Lee, R. E. Structural studies of pterin-based inhibitors of dihydropteroate synthase. *J. Med. Chem.* **2010**, *53*, 166−177.

(10) Frey, K. M.; Liu, J.; Lombardo, M. N.; Bolstad, D. B.; Wright, D. L.; Anderson, A. C. Crystal structures of wild-type and mutant methicillin-resistant *Staphylococcus aureus* dihydrofolate reductase reveal an alternate conformation of NADPH that may be linked to trimethoprim resistance. *J. Mol. Biol.* **2009**, *387*, 1298−1308.

(11) Bourne, C. R.; Bunce, R. A.; Bourne, P. C.; Berlin, K. D.; Barrow, E. W.; Barrow, W. W. Crystal structure of *Bacillus anthracis* dihydrofolate reductase with the dihydrophthalazine-based trimethoprim derivative RAB1 provides a structural explanation of potency and selectivity. *Antimicrob. Agents Chemother.* **2009**, *53*, 3065−3073.

(12) Yun, M. K.; Wu, Y.; Li, Z.; Zhao, Y.; Waddell, M. B.; Ferreira, A. M.; Lee, R. E.; Bashford, D.; White, S. W. Catalysis and sulfa drug resistance in dihydropteroate synthase. *Science* **2012**, *335*, 1110−1114.

(13) Zhao, Y.; Hammoudeh, D.; Yun, M. K.; Qi, J.; White, S. W.; Lee, R. E. Structure-based design of novel pyrimido[4,5-c]pyridazine derivatives as dihydropteroate synthase inhibitors with increased affinity. *ChemMedChem.* **2012**, *7*, 861−870.

(14) Hammoudeh, D. I.; Date, M.; Yun, M. K.; Zhang, W.; Boyd, V. A.; Viacava Follis, A.; Griffith, E.; Lee, R. E.; Bashford, D.; White, S. W. Identification and characterization of an allosteric inhibitory site on dihydropteroate synthase. *ACS Chem. Biol.* **2014**, 1294−1302.

(15) Haruki, H.; Pedersen, M. G.; Gorska, K. I.; Pojer, F.; Johnsson, K. Tetrahydrobiopterin biosynthesis as an off-target of sulfa drugs. *Science* **2013**, *340*, 987−91.

(16) Kluytmans-Vandenbergh, M. F.; Kluytmans, J. A. Community-acquired methicillin-resistant *Staphylococcus aureus*: current perspectives. *Clin. Microbiol. Infect.* **2006**, *12*, 9−15.

(17) Kollef, M. H.; Micek, S. T. Methicillin-resistant *Staphylococcus aureus*: a new community-acquired pathogen? *Curr. Opin. Infect. Dis.* **2006**, *19*, 161−168.

(18) Ohlsen, K.; Lorenz, U. Novel targets for antibiotics in *Staphylococcus aureus*. *Future Microbiol.* **2007**, *2*, 655−666.

(19) Spaulding, A. R.; Salgado-Pabon, W.; Merriman, J. A.; Stach, C. S.; Ji, Y.; Gillman, A. N.; Peterson, M. L.; Schlievert, P. M. Vaccination against *Staphylococcus aureus* pneumonia. *J. Infect. Dis.* **2014**, *209*, 1955−1962.

(20) Chhabra, S.; Barlow, N.; Dolezal, O.; Hattarki, M. K.; Newman, J.; Peat, T. S.; Graham, B.; Swarbrick, J. D. Exploring the chemical space around 8-mercaptoguanine as a route to new inhibitors of the folate biosynthesis enzyme HPPK. *PLoS One* **2013**, *8*, e59535.

(21) Chhabra, S.; Dolezal, O.; Collins, B. M.; Newman, J.; Simpson, J. S.; Macreadie, I. G.; Fernley, R.; Peat, T. S.; Swarbrick, J. D. Structure of *S. aureus* HPPK and the discovery of a new substrate site inhibitor. *PLoS One* **2012**, *7*, e29444.

(22) Derrick, J. P. The structure and mechanism of 6-hydroxymethyl-7,8-dihydropterin pyrophosphokinase. *Vitam. Horm.* **2008**, *79*, 411−433.

(23) Blaszczyk, J.; Shi, G.; Li, Y.; Yan, H.; Ji, X. Reaction trajectory of pyrophosphoryl transfer catalyzed by 6-hydroxymethyl-7,8-dihydropterin pyrophosphokinase. *Structure* **2004**, *12*, 467−475.

(24) Xiao, B.; Shi, G.; Gao, J.; Blaszczyk, J.; Liu, Q.; Ji, X.; Yan, H. Unusual conformational changes in 6-hydroxymethyl-7,8-dihydropterin pyrophosphokinase as revealed by X-ray crystallography and NMR. *J. Biol. Chem.* **2001**, *276*, 40274−40281.

(25) Garcon, A.; Levy, C.; Derrick, J. P. Crystal structure of the bifunctional dihydroneopterin aldolase/6-hydroxymethyl-7,8-dihydropterin pyrophosphokinase from *Streptococcus pneumoniae*. *J. Mol. Biol.* **2006**, *360*, 644−653.

(26) Hennig, M.; Dale, G. E.; D'Arcy, A.; Danel, F.; Fischer, S.; Gray, C. P.; Jolidon, S.; Muller, F.; Page, M. G.; Pattison, P.; Oefner, C. The structure and function of the 6-hydroxymethyl-7,8-dihydropterin pyrophosphokinase from *Haemophilus influenzae*. *J. Mol. Biol.* **1999**, *287*, 211−219.

(27) Lawrence, M. C.; Iliades, P.; Fernley, R. T.; Berglez, J.; Pilling, P. A.; Macreadie, I. G. The three-dimensional structure of the bifunctional 6-hydroxymethyl-7,8-dihydropterin pyrophosphokinase/dihydropteroate synthase of *Saccharomyces cerevisiae*. *J. Mol. Biol.* **2005**, *348*, 655−670.

(28) Xiao, B.; Shi, G.; Chen, X.; Yan, H.; Ji, X. Crystal structure of 6-hydroxymethyl-7,8-dihydropterin pyrophosphokinase, a potential target for the development of novel antimicrobial agents. *Structure* **1999**, *7*, 489−496.

(29) Wood, H. C. S. Specific inhibition of dihydrofolate biosynthesis—a new approach to chemotherapy. In *Chemistry and Biology of Pteridines*; Pfleiderer, W., Ed.; Walter de Gruyter: New York, 1975.

(30) Shi, G.; Blaszczyk, J.; Ji, X.; Yan, H. Bisubstrate analogue inhibitors of 6-hydroxymethyl-7,8-dihydropterin pyrophosphokinase: synthesis and biochemical and crystallographic studies. *J. Med. Chem.* **2001**, *44*, 1364−1371.

(31) Shi, G.; Shaw, G.; Li, Y.; Wu, Y.; Yan, H.; Ji, X. Bisubstrate analog inhibitors of 6-hydroxymethyl-7,8-dihydropterin pyrophosphokinase:

new lead exhibits a distinct binding mode. *Bioorg. Med. Chem.* **2012**, *20*, 4303−4309.
(32) Shi, G.; Shaw, G.; Liang, Y. H.; Subburaman, P.; Li, Y.; Wu, Y.; Yan, H.; Ji, X. Bisubstrate analogue inhibitors of 6-hydroxymethyl-7,8-dihydropterin pyrophosphokinase: new design with improved properties. *Bioorg. Med. Chem.* **2012**, *20*, 47−57.
(33) Bourne, C. R. Utility of the biosynthetic folate pathway for targets in antimicrobial discovery. *Antibiotics* **2014**, *3*, 28.
(34) Stammers, D. K.; Achari, A.; Somers, D. O.; Bryant, P. K.; Rosemond, J.; Scott, D. L.; Champness, J. N. 2.0 Å X-ray structure of the ternary complex of 7,8-dihydro-6-hydroxymethylpterinpyrophosphokinase from *Escherichia coli* with ATP and a substrate analogue. *FEBS Lett.* **1999**, *456*, 49−53.
(35) Williamson, M. P. Using chemical shift perturbation to characterise ligand binding. *Prog. Nucl. Magn. Reson. Spectrosc.* **2013**, *73*, 1−16.
(36) Medek, A.; Hajduk, P. J.; Mack, J.; Fesik, S. W. The use of differential chemical shifts for determining the binding site location and orientation of protein-bound ligands. *J. Am. Chem. Soc.* **2000**, *122*, 1241−1242.
(37) Lescop, E.; Lu, Z.; Liu, Q.; Xu, H.; Li, G.; Xia, B.; Yan, H.; Jin, C. Dynamics of the conformational transitions in the assembling of the Michaelis complex of a bisubstrate enzyme: a ^{15}N relaxation study of *Escherichia coli* 6-hydroxymethyl-7,8-dihydropterin pyrophosphokinase. *Biochemistry* **2009**, *48*, 302−312.
(38) Yang, R.; Lee, M. C.; Yan, H.; Duan, Y. Loop conformation and dynamics of the *Escherichia coli* HPPK apo-enzyme and its binary complex with MgATP. *Biophys. J.* **2005**, *89*, 95−106.
(39) Iwaoka, M.; Isozumi, N. Hypervalent nonbonded interactions of a divalent sulfur atom. Implications in protein architecture and the functions. *Molecules* **2012**, *17*, 7266−7283.
(40) Blaszczyk, J.; Shi, G.; Yan, H.; Ji, X. Catalytic center assembly of HPPK as revealed by the crystal structure of a ternary complex at 1.25 Å resolution. *Structure* **2000**, *8*, 1049−1058.
(41) Yun, M. K.; Hoagland, D.; Kumar, G.; Waddell, M. B.; Rock, C. O.; Lee, R. E.; White, S. W. The identification, analysis and structure-based development of novel inhibitors of 6-hydroxymethyl-7,8-dihydropterin pyrophosphokinase. *Bioorg. Med. Chem.* **2014**, *22*, 2157−2165.
(42) Zhou, P.; Zou, J. W.; Tian, F. F.; Shang, Z. C. Fluorine bonding - how does it work in protein-ligand interactions? *J. Chem. Inf. Model.* **2009**, *49*, 2344−2355.
(43) Veber, D. F.; Johnson, S. R.; Cheng, H. Y.; Smith, B. R.; Ward, K. W.; Kopple, K. D. Molecular properties that influence the oral bioavailability of drug candidates. *J. Med. Chem.* **2002**, *45*, 2615−2623.
(44) Chhabra, S.; Newman, J.; Peat, T. S.; Fernley, R. T.; Caine, J.; Simpson, J. S.; Swarbrick, J. D. Crystallization and preliminary X-ray analysis of 6-hydroxymethyl-7,8-dihydropterin pyrophosphokinase from *Staphylococcus aureus*. *Acta Crystallogr., Sect. F: Struct. Biol. Cryst. Commun.* **2010**, *66*, 575−578.
(45) Delaglio, F.; Grzesiek, S.; Vuister, G. W.; Zhu, G.; Pfeifer, J.; Bax, A. NMRPipe: a multidimensional spectral processing system based on UNIX pipes. *J. Biomol. NMR* **1995**, *6*, 277−293.
(46) Bartels, C.; Xia, T. H.; Billeter, M.; Guntert, P.; Wuthrich, K. The program XEASY for computer-supported NMR spectral analysis of biological macromolecules. *J. Biomol. NMR* **1995**, *6*, 1−10.
(47) Goddard, T. D.; Kneller, D. G. *SPARKY 3*; University of California: San Francisco, CA.
(48) Kabsch, W. XDS. *Acta Crystallogr., Sect. D: Biol. Crystallogr.* **2010**, *66*, 125−32.
(49) Collaborative Computational Project, Number 4. The CCP4 suite: programs for protein crystallography. *Acta Crystallogr., Sect. D: Biol. Crystallogr.* **1994**, *50*, 760−763.
(50) Storoni, L. C.; McCoy, A. J.; Read, R. J. Likelihood-enhanced fast rotation functions. *Acta Crystallogr., Sect. D: Biol. Crystallogr.* **2004**, *60*, 432−438.
(51) Murshudov, G. N.; Vagin, A. A.; Dodson, E. J. Refinement of macromolecular structures by the maximum-likelihood method. *Acta Crystallogr., Sect. D: Biol. Crystallogr.* **1997**, *53*, 240−255.
(52) Emsley, P.; Cowtan, K. Coot: model-building tools for molecular graphics. *Acta Crystallogr., Sect. D: Biol. Crystallogr.* **2004**, *60*, 2126−2132.
(53) Kimple, A. J.; Muller, R. E.; Siderovski, D. P.; Willard, F. S. A capture coupling method for the covalent immobilization of hexahistidine tagged proteins for surface plasmon resonance. *Methods Mol. Biol.* **2010**, *627*, 91−100.
(54) *Maestro, version 9.7*; Schrödinger, LLC: New York, 2014.
(55) *Schrödinger Suite 2014-1: Protein Preparation Wizard, Epik version 2.7, Impact version 6.2, Prime version 3.4*; Schrödinger, LLC: New York, 2014.
(56) *LigPrep*; Schrödinger, LLC: New York, 2014.
(57) Friesner, R. A.; Murphy, R. B.; Repasky, M. P.; Frye, L. L.; Greenwood, J. R.; Halgren, T. A.; Sanschagrin, P. C.; Mainz, D. T. Extra precision glide: docking and scoring incorporating a model of hydrophobic enclosure for protein-ligand complexes. *J. Med. Chem.* **2006**, *49*, 6177−6196.